Experiments and modelling of choked flow of CO_2 in orifices and nozzles

Morten Hammer[a], Han Deng[a], Anders Austegard[a], Alexandra Metallinou Log[b], Svend Tollak Munkejord[a,*]

[a] *SINTEF Energy Research, P.O. Box 4761 Torgarden, NO-7465 Trondheim, Norway*
[b] *Norwegian University of Science and Technology, Department of Energy and Process Engineering, NO-7491 Trondheim, Norway*

Abstract

In order to accelerate the deployment of CO_2 capture and storage (CCS), engineers need experimentally validated models, among other things, to predict the mass flow rate in process equipment and flow restrictions like valves, nozzles and orifices. There are few available, relevant data for choked CO_2 flow in such geometries. To amend the situation, in this work, we report on six pipe-depressurization experiments from a pressure of 12 MPa and a temperature of 25 °C through three sizes (4.5, 9.0 and 12.7 mm) of orifices and nozzles. The results indicate that for the present cases, the choke point is at a non-equilibrium state.

In order to predict quasi-steady choked flow in restrictions, the homogeneous equilibrium model (HEM) and the Henry–Fauske (HF) model are commonly used. The HEM often underpredicts the mass flow rate because it does not account for delayed phase transition. Here we develop a delayed HEM (D-HEM) where evaporation starts at the superheat limit described using classical nucleation theory. We then employ the HEM, D-HEM, and HF model in 1D CFD pipe simulations to describe the outflow of depressurization experiments and we also compare with experimental data for converging-diverging nozzles.

In the CFD simulations, HF gave the best results, while HEM consistently underpredicted the mass flux. For the nozzle calculations, we found D-HEM to be the best model with a relative absolute error of 2.5 % for the predicted mass flux.

Keywords: carbon dioxide, depressurization, decompression, critical flow, nucleation, thermodynamics, fluid dynamics

*Corresponding author.
Email address: svend.t.munkejord [a] sintef.no (Svend Tollak Munkejord)

Nomenclature

Latin letters

A Area . . . . . m^2
c Speed of sound . . . . . m/s
C_C Contraction coefficient 1
d Diameter . . . . . m
E Total energy . . . . . J/m^3
e Specific internal energy . . . . . J/kg
$\boldsymbol{F}$ Flux vector . . . . . -
$\mathcal{F}$ Friction force . . . . . N/m^3
G Free energy . . . . . J
H Enthalpy . . . . . J
h Specific enthalpy . . . . . J/kg
j Mass flux . . . . . $kg/(m^2\,s)$
J Nucleation rate . . . . . $1/(m^3\,s)$
K Kinetic prefactor . . . . . $1/(m^3\,s)$
k_B Boltzmann's constant . . . . . J/K
l and L Length . . . . . m
m Mass . . . . . kg
$\dot{m}$ Mass flow rate . . . . . kg/s
N Mol number . . . . . mol
P Pressure . . . . . Pa
Q Heat . . . . . W/m^3
r Radius . . . . . m
S Entropy . . . . . J/K
s Specific entropy . . . . . J/(K kg)
T Temperature . . . . . K
t Time . . . . . s
u Velocity . . . . . m/s
V Volume . . . . . m^3
x Spatial coordinate . . . . . m
z Mass fraction . . . . . kg/kg

Greek letters

α Volume fraction . . . . . m^3/m^3
β Restriction angle parameter, Fig. 3 . . . . . °
δ Orifice opening length parameter, Fig. 3 . . . . . m
μ Chemical potential . . . . . J/mol
ρ Density . . . . . kg/m^3
$\tilde{\rho}$ Number density . . . . . $1/m^3$
σ Surface tension . . . . . N/m

Subscripts

amb Ambient
cons Conserved
crit Critical
b Cell at end of inner pipe domain adjacent the restriction

g Gas
ℓ Liquid
pipe Position inside pipe
res Restriction
sat Saturation
up Upstream
vc Vena contracta
w Wall

Superscripts
* Critically-sized embryo

Abbreviations
CCS CO_2 capture and storage
CFD Computational fluid dynamics
CNT Classical nucleation theory
DEM Delayed equilibrium model
D-HEM Delayed homogeneous equilibrium model
EOS Equation of state
HEM Homogeneous equilibrium model
HF Henry–Fauske
HRM Homogeneous relaxation model
RDF Running ductile fracture
SHL Superheat limit

1. Introduction

There is consensus that in order to mitigate climate change, CO_2 capture and storage (CCS) is one of the necessary tools (Edenhofer *et al.*, 2014). In the IEA (2021) scenario to reach net zero emissions by 2050, 7.6 gigatonnes of CO_2 are captured globally per year, out of which 95 % is permanently stored. Because capture plants and storage sites are in general not colocated, a large-scale CO_2-transportation system needs to be deployed, including pipelines and ships. In designing, optimizing and operating these systems, engineers need to quantify processes and phenomena that are not all covered by standard engineering tools (Munkejord *et al.*, 2016). This includes the tight coupling of fluid and thermodynamics due to the proximity of the operating conditions to both the critical point (above which there is only one phase) and the triple point (at which gas, liquid and solid coexist). One practically important topic is to predict the mass flow rate in flow restrictions like valves, nozzles and orifices, both inside process equipment and in case of leaks to the surroundings.

When a fluid is depressurized through a restriction, the flow will become sonic if the pressure difference is sufficiently large. This is called critical or choked flow (Chapman, 2000). For sonic flow, there are no waves travelling upstream and therefore no feedback from the downstream pressure, so that the flow rate becomes independent of the downstream conditions. The correct prediction of critical flow is relevant not only for CCS systems, but also refrigeration systems (Angielczyk *et al.*, 2010, 2019, 2020; Banasiak and Hafner, 2013; Ringstad *et al.*, 2020), nuclear reactor

safety (Downar-Zapolski *et al.*, 1996; Pinhasi *et al.*, 2005; De Lorenzo *et al.*, 2017) and in other industrial facilities involving pressurized fluids.

In ship transportation, the CO_2 will be in a cold liquid state (Roussanaly *et al.*, 2021), whereas in pipelines, it will most often be in a dense liquid phase at super-critical pressures (Munkejord *et al.*, 2016). On depressurization from these states, the liquid will evaporate, and solid CO_2 will be formed at the triple point (see e.g. Hammer *et al.*, 2013). For such systems, valid critical-flow models are needed for correct sizing of valves used for pressure reduction. The discharge mass flow rate influences the depressurization rate of the system and impacts both the time to empty it and the minimum temperature reached during depressurization.

During depressurization of liquids or dense-phase fluids, delayed phase transition and the presence of metastable states is a well known phenomenon (Liao and Lucas, 2017), and departure from chemical and thermal equilibrium between the phases must be accounted for. It is known that non-equilibrium flow models predict higher characteristic speeds which in turn gives a higher critical mass flow rate (Flåtten and Lund, 2011). Therefore, models like the often-used homogeneous equilibrium model (HEM) that assume full equilibrium (mechanical, thermal and chemical) are expected to underpredict the critical mass flow rate. Nevertheless, we have obtained good results using the HEM for situations where the characteristic speeds are not determining (Munkejord *et al.*, 2020).

Departure from equilibrium is also relevant for the correct prediction of running ductile fracture (RDF), a phenomenon whereby a defect in the pipeline, caused by e.g. corrosion or external forces, develops into a fracture running along the pipe, sustained by the pressure forces from the escaping fluid, see Aursand *et al.* (2016a). Assuming full equilibrium will yield higher-than-realistic pressures and therefore a wrong evaluation of the forces impacting the steel, see Munkejord *et al.* (2020).

In order to model CO_2 flows out of equilibrium, the process of nucleation must be taken into account. Shin and Jones (1993) and Blinkov *et al.* (1993) modelled the effect of heterogeneous nucleation on the wall and in the bulk of the fluid for water flowing through a converging-diverging nozzle. This work required empirical correlations to describe the heterogeneous nucleation of bubbles on the nozzle surface and impurities present in the bulk liquid. Their approach required an involved integration over time and space and provided promising results. In the present paper, the effect of heterogeneous nucleation is not included as the CO_2 depressurization experiments studied are in the entropy region where spontaneous *homogeneous* nucleation is the dominant mode of nucleation. This kind of nucleation occurs in the bulk of the liquid without the aid of a surface or impurity, and it relates closely to the limit of superheat, i.e., the experimentally attainable limit where a superheated liquid spontaneously starts boiling. This is further discussed in Section 3.3.

Following the approach presented by Debenedetti (1997, Sec. 3.1.5), Aursand *et al.* (2016b) concluded that the superheat limit (SHL) of a fluid can be accurately predicted by the use of classical nucleation theory (CNT). The CNT predictions depend mainly on the saturation pressure and surface tension of the fluid, and in order to predict the SHL, accurate models for both properties are required. Aursand and Hammer (2018) employed the CNT models to predict rapid phase transition for liquefied natural gas. For liquid and dense-phase specific entropies close to, but

below, the critical entropy, Wilhelmsen and Aasen (2022) applied CNT to describe delayed phase transition for flows of water, and CO_2, in converging nozzles. At lower temperatures (below about 280 K) and entropies, heterogeneous nucleation becomes more important, and this effect was taken into account for water using an empirical correlation.

Elias and Lellouche (1994) reviewed two-phase critical flow models with emphasis on water-steam flows and nuclear reactor safety. The model review comprised 'analytical models' (models not requiring spatial or temporal integration) including the HEM and the models of Moody (1965) and Henry and Fauske (1971) (HF), fitted models, and steady-state two-phase flow models requiring spatial integration. The data review evaluated 42 data sets. Elias and Lellouche found that none of the analytical or fitted models satisfactorily captured the measured mass fluxes for the range of conditions considered.

De Lorenzo *et al.* (2017) benchmarked the delayed equilibrium model (DEM) and classical two-phase critical flow models against experimental data. In addition to the HEM they evaluated the Moody (1965) and HF models. The DEM originated from Lackme (1979) who assumed two-phase critical flow to be composed of three phases. In addition to saturated vapour, the flow model contained both a saturated and a metastable liquid. Assessing more than 450 experimental data points for three configurations, long tubes, short nozzles and slits, De Lorenzo *et al.* concluded that the DEM model was superior to the other models, and that HEM predicted the long tube critical flux well while HF overestimated the mass flux in the same geometry. Moody's model had too much slip and overestimated the mass flux for two-phase stagnation conditions.

The homogeneous relaxation model (HRM) takes into account the non-equilibrium evaporation leading to metastable liquid states. In this model, the phases have the same pressure and temperature, but are allowed to have different chemical potential. The model, as formulated by Downar-Zapolski *et al.* (1996), requires a relaxation time to account for time delay in the phase transition. Angielczyk *et al.* (2010) adapted the relaxation-time correlation developed for water by Downar-Zapolski *et al.* to work with CO_2 utilizing experimental data by Nakagawa *et al.* (2009). These experiments were performed using four different converging-diverging nozzles, with different angles in the diverging part. The fluid used was pure CO_2 that was expanded from a constant upstream pressure. The mass flow rate was estimated assuming a saturated state at the throat, but it was not tabulated by the authors. Brown *et al.* (2013) used the empirical correlation of Angielczyk *et al.* to describe the relaxation time in pipe depressurization simulations.

Common formulations of the DEM (De Lorenzo *et al.*, 2017) and HRM (Downar-Zapolski *et al.*, 1996) rely on time-dependent mass transfer between the phases, and require temporal as well as spatial integration over a fully defined geometry. This makes them less generic than the classical methods such as HEM and HF. The steady-state HEM flow can be determined without time integration and HF is a set of analytical equations. Modelling the restriction geometry in detail may be challenging, e.g., for simulations of long pipes, where the spatial resolution of the restriction is not resolved, or for cases where the geometry is partly unknown. Attempts have been made to devise robust numerical methods to simulate transient flow of CO_2 through pipes or ducts with *discontinuous* variation of the cross section (Brown

et al., 2015; Log *et al.*, 2021), but so far, these methods have only been applied to equilibrium flow models.

We have only found a limited amount of experimental data of CO_2 flowing through nozzles or orifices that include the mass flow rate and where the decompression path comes from the liquid side of the phase diagram. Hesson and Peck (1958) presented critical flow rates for saturated liquid and saturated vapour CO_2 for a nozzle and an orifice. Henry and Fauske (1971) used the data of Hesson and Peck when developing the HF model. However, Hendricks *et al.* (1972) questioned the accuracy of the Hesson and Peck data. The measured fluxes were found to be higher than expected, indicating that the liquid states were sub-cooled to some degree.

Martin *et al.* (2006) performed experiments of supercritical and liquid CO_2 with short tube orifices of length 20 mm and diameter 0.8 mm and 1 mm. The measured mass flow rate increased with increasing upstream pressure and decreasing temperature.

Edlebeck *et al.* (2014) reported a comprehensive data set for supercritical and two-phase CO_2 flowing through orifices. The orifices were of 1 mm diameter and length-to-diameter ratios of 3.2 and 5. Edlebeck *et al.* measured the mass flow rates for a wide range of initial conditions, and compared with the isentropic real gas model for fluid expansion through a nozzle. The comparison gave a discharge coefficient for single phase between 0.81 and 0.87.

Banasiak and Hafner (2013) experimentally measured the mass flow rate of dense-phase CO_2 in a converging-diverging nozzle used in ejectors. A nozzle flow model was presented, including delayed equilibrium accounting for both homogeneous and heterogeneous nucleation.

Vree *et al.* (2015) tested rapid depressurization of CO_2 through 3, 6, and 12 mm nozzles connected to a coil-shaped tube. Mass flow rates were reported, but not as a function of the upstream state. In a somewhat similar study, Li *et al.* (2016) experimentally investigated the leakage of CO_2 at supercritical pressures through nozzles of different shapes and sizes in the millimetre range. Fan *et al.* (2018) studied supercritical CO_2 leaking through nozzles with length-diameter ratio (L/D) ranging from 1 to 15. It was found that the choked mass flow rate decreased with increasing length-diameter ratio.

Pipe depressurizations through restrictions have implicit information on the mass flux through the measured pressure as long as the upstream state is single-phase. This can alleviate the lack of experiments with directly measured mass flow rates. The mass flux can be calculated using the Euler compatibility equation, as we will discuss in Section 3.1.

Armstrong and Allason (2014) conducted experiments in which a 200 m long pipe with inner diameter 50 mm was depressurized full-bore or through sharp orifice plates. Two of the experiments had a pipe aperture ratio low enough that the entire initial rarefaction wave remained in the single-phase region. Guo *et al.* (2016, 2017) and Yan *et al.* (2018) studied the depressurization of a large pipe of length 257 m and inner diameter 233 mm with full-bore opening and two orifices. They observed pressure transients attributed to phase change as pressure waves were reflected at the pipe ends. Martynov *et al.* (2018) studied the decompression of a 36.7 mm long pipe with internal diameter 50 mm through orifices of diameter 4 and 6 mm. The focus of the study was the formation of solid CO_2 at the triple point.

To sum up the state of the art, considerable work has been undertaken on critical flow through restrictions, but the main emphasis has been on geometries like converging-diverging nozzles. Among the studies on nozzles that we reviewed, only few could be directly used in the present model evaluation, e.g., reporting the upstream state so that the mass flow rate could be calculated. Further, there is a need to develop and validate models that are generic enough to be implemented in simulation tools for CCS applications such as pipes and vessels.

In this work, the decompression-tube facility described in Munkejord *et al.* (2020) has been equipped with interchangeable outflow restrictions. We thus present new critical-flow data for CO_2 exiting through sharp-edged orifices and converging nozzles. In addition to modelling the outflow using the classical HEM and HF models, we propose an augmented steady-state HEM (D-HEM) capturing the delayed phase transition and entropy production during mass transfer. These restricted-flow models are discussed both separately and as part of 1D CFD pipe simulations.

The rest of the article is structured as follows: Section 2 briefly describes the experimental setup and procedure. Section 3 presents the theoretical framework for analysing the experimental data, and the models used to predict the mass flux in the nozzle and orifice geometries. Section 4 presents experimental and simulation results, and discusses our observations. Section 5 summarizes the main results and conclusions.

2. Experimental setup

This section gives an overview of the experimental setup. A more detailed description can be found in Munkejord *et al.* (2020).

2.1. ECCSEL depressurization facility

The test section of the ECCSEL depressurization facility ECCSEL (2021) consists of a pipe equipped with a rupture disk at the open end and instrumented to observe the rapid pressure and temperature transients occurring during depressurization of CO_2 and CO_2-rich mixtures. It is connected to the gas supply with mass flow controllers, and the compression and cooling system for achieving the desired experimental conditions. Figure 1a shows a schematic overview. The maximum operating pressure of the facility is 20 MPa, and the current design allows experiments with initial temperatures in the range of 5 °C to 40 °C.

The test section is made of 11 stainless steel (SS316, EN 1.4401) pipes giving a total length of 61.67 m, as depicted in Figure 1b. The pipes have an inner diameter of 40.8 mm and outer diameter of 48.3 mm, and the internal surface of the pipes were honed to a mean roughness, R_a, in a range from 0.2 µm to 0.3 µm. In order to achieve a uniform axial temperature, the pipe is wrapped by self-regulating positive temperature coefficient (PTC) heating cables and insulated with a 60 mm thick glass wool layer. The power output of the heating cables is 1900 W at 20 °C and 950 W at 40 °C.

A rupture disk with a disk holder is installed at the pipe outlet. The specified burst pressure of the disk is 120 barg±5% at 22 °C. The depressurization is triggered once the disk ruptures. Two rupture disk types are employed in this study; X-scored

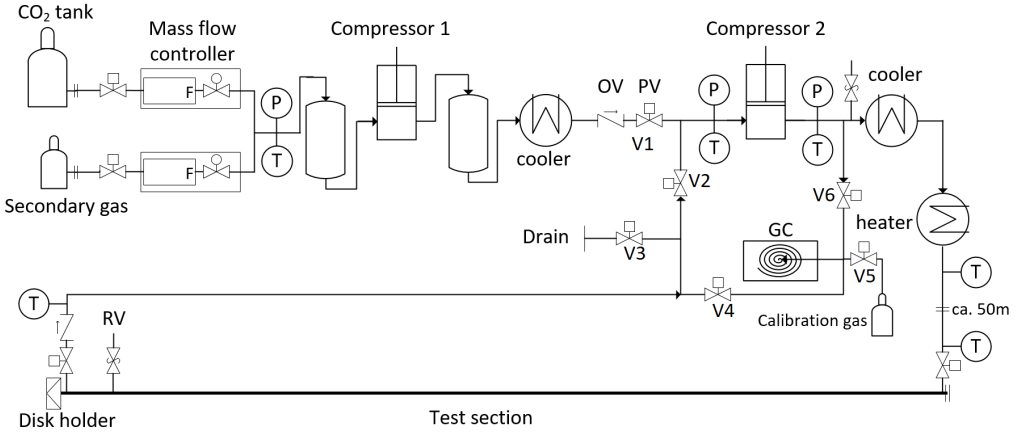

(a) System (RV: relief valve; OV: one-way valve; PV: pneumatic valve)

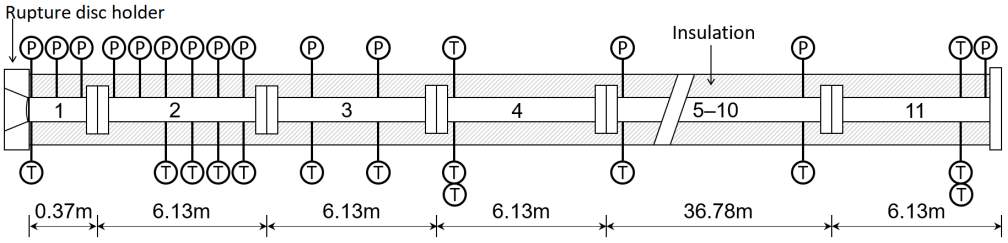

(b) Test section (dimensions are not to scale; pipe no. 5–10 and corresponding sensors are omitted.)

Figure 1: Schematic of the ECCSEL depressurization facility.

Fike SCRD BT FSR for Tests 8 and 13 and circular-scored triple-layer Fike HOV BT HL for the remaining experiments (Tests 16–18), see Table 2. A fully opened triple-layer disk is shown in Figure 2a.

In order to perform depressurization tests with different restrictions at the pipe outlet, we manufactured a series of screw-in tubes with orifice and nozzle profiles, as illustrated in Figure 3. The dimensions are given in Table 1. In the current work, three restriction diameters, 4.5 mm, 9.0 mm and 12.7 mm, are employed for both the orifice and nozzle geometry. The screw-in tube, depicted in Figure 2b for the 12.7 mm nozzle, is mounted immediately upstream of the rupture disk. The design is such that the flow will choke at the same position as in the full-bore experiments reported in Munkejord *et al.* (2020, 2021).

2.2. Instrumentation and test procedure

Along the test section, 16 fast-response pressure transducers of model Kulite CTL-190(M) are flush-mounted to the internal surface. Most of them are densely distributed close to the rupture disk to capture the decompression wave, as depicted in Figure 1b. The fluid temperature is measured by 23 Type E thermocouples. The measurement uncertainty of pressure is ±60 kPa and temperature uncertainty is ±0.22 °C, both with a confidence level of 95 %. In the present work, we focus on

(a) Triple-layer rupture disk after test.

(b) Converging nozzle of 12.7 mm diameter.

Figure 2: Pictures of rupture disk and converging nozzle.

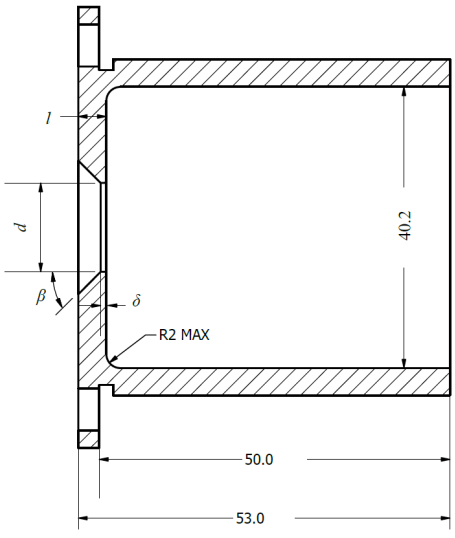

(a) Orifice

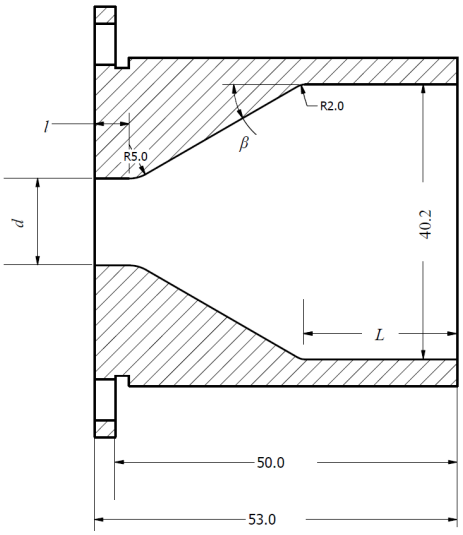

(b) Converging nozzle

Figure 3: Schematic of orifice and converging nozzle. The flow direction is from the right to the left.

Table 1: Geometry of the orifices and nozzles used for our experiments.

	Test no.	d (mm)	l (mm)	β (°)	δ (mm)	L (mm)
Orifice, large	13	12.7	4	45	0.8	–
Orifice, medium	21	9.0	4	45	0.8	–
Orifice, small	16	4.5	4	45	0.8	–
Nozzle, large	18	12.7	5	30	–	22.3
Nozzle, medium	20	9.0	4	35	–	24.5
Nozzle, small	17	4.5	3	45	–	29.3

investigation of the outflow, thus only the data recorded at the position closest to the outlet, at the location of 0.08 m, will be presented. Details regarding sensor location, calibration, and uncertainty analysis can be found in Munkejord *et al.* (2020).

The logging frequency of the data from the pressure transducers and thermocouples is 100 kHz and 1 kHz, respectively. The high-frequency data are stored from 0.3 s before disk rupture for a 9 s period. Afterwards, both pressure and temperature data are recorded at 50 Hz. The reported initial conditions of the experiments are calculated from the data between 1 ms and 0.5 ms before disk rupture.

The experimental procedure involves the following steps. First, the rupture disk is installed and the system is evacuated. Then the test section is filled with CO_2 and pressurized. When the pressure reaches about 70% of the desired pressure, the fluid is circulated to achieve a uniform temperature along the test section. The fluid temperature is controlled using heating elements wrapped around the test section. The desired pressure and temperature are achieved by further heating and addition of CO_2 if needed, both at a controlled rate, until the disk ruptures. Upon disk rupture, the two pneumatic valves at the ends of the test section are automatically closed to stop circulation. After the test, the system is emptied.

3. Models

In this section, we start by describing how the mass flow-rate can be computed from pressure data of a depressurization experiment. Next, we give a short description of the thermophysical models used in this work. We then discuss how classical nucleation theory can be applied to calculate the superheat limit, which is used for delayed phase transition considerations in steady-state critical flow models. Finally, we describe the model used for calculating the vena contracta area reduction of the orifice and we give an outline of the 1D CFD model used for the simulations.

3.1. The Euler compatibility equation for the rarefaction wave

When the rupture disk at the end of the pipe opens, flow is established through the outlet restriction, and a rarefaction wave starts travelling into the pipe. The mass flow rate will depend on the size of the restriction and the fluid state inside the pipe, close to the outlet. After a short initial time, allowing for the fluid to accelerate through the restriction, a quasi-steady state is established, where the flow through the restriction is constant and a pressure plateau (P_1) is established in the pipe with a constant mass flow rate downstream of the rarefaction wave, see Figure 4.

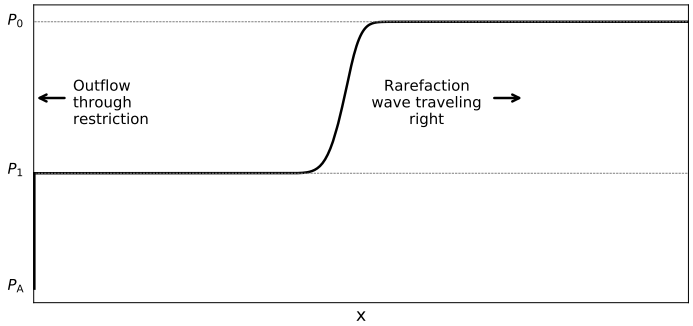

Figure 4: Example of an adiabatic pipe depressurization trough a restriction on the left side. The pressure in the pipeline is plotted against axial position for a given time. The initial pipe pressure is P_0 and the pressure drops to P_1 due to the outlet flow. P_A is the ambient pressure.

The change in fluid velocity across a rarefaction wave in a single-phase fluid can be described using a compatibility equation of the Euler equations (Picard and Bishnoi, 1988).

The compatibility equations are found when rewriting the original differential equations along the characteristics. The sudden outflow constitutes an event opposite of a hydraulic shock (often referred to as 'fluid hammer' or 'water hammer'), and the compatibility equation is equivalent to the Joukowsky equation used to analyse such events. Using only the pressure measurements and an accurate equation of state (EOS) for the fluid properties, we can calculate the constant velocity in the pipe. The Euler compatibility equation for the rarefaction wave states that, at constant entropy,

$$\mathrm{d}P = \rho c \mathrm{d}u. \tag{1}$$

Knowing the initial pressure, P_0, the initial velocity, $u_0 = 0$, and plateau pressure, P_1, from the experiments, we can integrate the equation (1) to find the velocity behind the rarefaction wave in the pipe as

$$u_1 = \int_{P_0}^{P_1} \frac{\mathrm{d}P}{\rho c}. \tag{2}$$

The mass flow rate corresponding to the change in pressure can then be calculated from the fluid velocity and the fluid properties as $\dot{m} = (u\rho)_1 A_{\mathrm{pipe}}$. For single-phase flow, the density, $\rho(s, P)$, and speed of sound, $c(s, P)$, can be calculated from an equation of state given the entropy (s) and pressure.

3.2. Thermophysical models

For the calculation of thermophysical properties, we employ our in-house framework (Wilhelmsen *et al.*, 2017; Hammer *et al.*, 2020). To describe the thermodynamic properties of pure CO_2, we have utilized the GERG-2008 (Kunz and Wagner, 2012) and the Span and Wagner (1996) EOS, which are highly accurate Helmholtz-type

EOSs. GERG-2008 is developed for mixtures, but when employed for pure CO_2, it will give very similar predictions to those of the more accurate Span–Wagner EOS. The main difference will be in the close proximity of the critical point, where the Span–Wagner EOS has some enhancement terms. The EOSs are used to calculate the densities and energies of the existing phases in both the stable and metastable region. The development of the GERG-2008 and Span–Wagner EOS was purely based on experimental measurements of stable thermodynamic states. In addition, these EOSs exhibit an additional unphysical Maxwell-loop in the unstable area (Wilhelmsen *et al.*, 2017).

The accuracy in the metastable liquid region and the accuracy in predicting the spinodal curve is therefore unknown. Alternative equations of state based on statistical thermodynamics are expected to be more physically correct in the metastable region. However, the density and speed-of-sound predictions of GERG-2008 and Span–Wagner EOS are far superior in the stable domain compared to alternative EOSs, and they are therefore used in this work. How far the better predictions will extend into the metastable region is unknown.

To calculate the CO_2 surface tension we employ the correlation of Rathjen and Straub (1977), and the viscosity is modelled using the correlation of Fenghour *et al.* (1998).

3.3. Estimating the liquid superheat limit using classical nucleation theory

Before describing restricted-flow models accounting for delayed phase transition, it is useful to define what we mean by the SHL. When a liquid reaches its superheat limit, random fluctuations of density will cause the formation of critically-sized gas bubbles that can grow due to evaporation on the gas-liquid interface or by coalescing with other bubbles. The formation of critically-sized embryos in a metastable phase is called nucleation. This is an activated process, meaning that a certain free-energy barrier must be overcome to form embryos of the new phase. If nucleation occurs spontaneously within the bulk of the fluid, it is called *homogeneous*. On the other hand, if nucleation occurs on a surface or an impurity such that the free-energy barrier is lowered, it is called *heterogeneous*. Heterogeneous nucleation dominates at lower temperatures, whereas homogeneous nucleation dominates at higher temperatures.

The data which we will analyse are mostly in the high-temperature region. Therefore, we consider the model presented by Aursand *et al.* (2016b) to estimate the homogeneous liquid superheat limit. This model is based on CNT, as described by Debenedetti (1997), in which the nucleation rate (critically-sized embryos formed per volume and time) is defined as an Arrhenius-type rate law,

$$J = K \exp\left(-\frac{\Delta G^*}{k_B T_\ell}\right), \tag{3}$$

where ΔG is the free-energy barrier of embryo formation, k_B is the Boltzmann constant and K is a kinetic prefactor. The superscript $*$ denotes properties of a critically-sized embryo. Such embryos are just large enough to not spontaneously decompose back to the mother phase. The free-energy barrier is estimated to be

$$\Delta G^* = \frac{4\pi\sigma r^{*2}}{3}, \tag{4}$$

where σ denotes the surface tension and r the radius of the embryo. It is assumed that the surface tension of the embryo, σ, is equal to the macroscopic surface tension of a planar interface between the phases at equilibrium.

For the formation of bubbles in a metastable liquid, the critical radius is approximated as

$$r^* = \frac{2\sigma}{P_{\text{sat}}(T_\ell) - P_\ell}, \tag{5}$$

where $P_{\text{sat}}(T_\ell)$ is the saturation pressure at the temperature of the liquid. The kinetic prefactor can be approximated as

$$K = \tilde{\rho}_\ell \sqrt{\frac{2\sigma}{\pi m}}, \tag{6}$$

where m is the mass of one molecule and $\tilde{\rho}_\ell = \rho_\ell / m$ is the number density of molecules in the liquid. With these relations, the SHL temperature can be estimated by solving

$$J(T_\ell) = J_{\text{crit}} \tag{7}$$

for T_ℓ. Here, J_{crit} is the critical nucleation rate, at which sudden phase change is observed (Aursand *et al.*, 2016b). In this work, we follow Aursand *et al.* (2016b), employing $J_{\text{crit}} = 1 \times 10^{12} / (\text{m}^3\,\text{s})$. Due to the exponential functional form in (3), the superheat limit is not very sensitive to the critical rate.

The SHL curve for CO_2 is plotted in Figure 5a, and it will always lie between the saturation curve and the spinodal curve. The spinodal curve of a pure fluid is the loci of $\frac{\partial P}{\partial \rho}\big|_T = 0$, which is a property predicted by the GERG-2008 EOS.

3.4. Steady-state flow through restrictions

To model flow through restrictions while avoiding detailed spatial and temporal integration, one must resort to steady-state flow modelling and ignore friction. This is reasonable for many practical applications. The fluid velocity, u, is then calculated from energy conservation under isentropic expansion, i.e., constant stagnation enthalpy,

$$h + \frac{1}{2}u^2 = C, \tag{8}$$

where C is a constant. When the difference between the upstream pressure (P_{up}) and the downstream pressure (P_{amb}) is sufficiently large, the flow will choke when the velocity equals the speed of sound on the calculated path, see the example for HEM in Appendix B. Otherwise, the flow will remain subsonic and the flow rate is determined from (8) and the downstream pressure. In any case, the main output from the restricted-flow model is the mass flux

$$j_{\text{res}} = (\rho u)_{\text{res}} = j_{\text{res}}\left(u_{\text{up}}, s_{\text{up}}, P_{\text{up}}, P_{\text{amb}}\right). \tag{9}$$

The above equations (8) and (9) have been formulated for equilibrium flow for simplicity. It is possible to extend them to non-equilibrium conditions if needed.

In the cases we consider here, at a certain point between the upstream and the ambient conditions, a two-phase state will be encountered. It is straightforward to

write the HEM as a steady-state model, only requiring isentropic path calculations. The HEM assumes full equilibrium (mechanical, thermal and chemical) between the gas and the liquid phase. As a consequence, the calculated speed of sound is discontinuous at the saturation curve.

The Henry and Fauske (1971) model incorporates some departure from equilibrium, and the flashing at the throat is correlated against the equilibrium flashing of the liquid. In the HF model, the liquid phase is treated as incompressible, while the gas is approximated as polytropic, with a polytropic exponent calculated assuming thermal equilibrium between the gas and the liquid. For the experiments in this work, the upstream gas fraction is always zero, so we need not discuss the approximate gas properties description in the HF model. To calculate $j_{\mathrm{res}}^{\mathrm{HF}}$, we solve Equation (45) of Henry and Fauske (1971) numerically.

Most models that include some delayed flashing, like the DEM and HRM, require that the flow be integrated over the nozzle geometry. As the geometry in many cases is complex or partly unknown, engineering process and pipe-flow simulators often rely on correlations or models like HEM and HF to describe flow rates in valves and nozzles based only on information of flow area and a discharge or contraction coefficient. If a valve flow coefficient is specified, in order to predict the flow rate, we must convert the flow coefficient to an equivalent flow area. In the following section, we propose a model including delayed flashing that does not require integration over the geometry.

3.5. Delayed homogeneous equilibrium model

In rarefaction-wave measurements from full-bore depressurization experiments of CO_2, one can observe a process where the fluid first experiences delayed phase transition, and then shows an equilibrium-like behaviour after an intermediate transition region (Munkejord *et al.*, 2020, Figs. 14 and 15). The same experimental data are plotted in Figure 8. In order to model the process, we will as a first approximation ignore the behaviour in this intermediate region (seen for $c - u$ between 280 m/s and 360 m/s in Figure 8b).

We next assume that the fluid experiences some delayed phase transition activated at the SHL and transitions into equilibrium flow at the SHL pressure. We then get a simple model that captures at least some of the observed essential physics. The energy is conserved during this process, and the fluid velocity given by the equation (8) should be continuous. This leads to a process of constant enthalpy at the SHL pressure. We note that the assumption of a process of constant pressure after the SHL is likely a simplification because the pressure has been observed to increase in pipe experiments when rapid evaporation follows delayed phase transition (Munkejord *et al.*, 2020, Figure 8, Sensor PT203).

The above approach is a steady-state delayed homogeneous equilibrium model, which we label D-HEM. In summary, the process steps of the model are illustrated in Figures 5a and 5b for the pressure-temperature and pressure-entropy space, respectively:

- Point 1 is the fluid state upstream of the restriction.
- Point 2 is reached by isentropic expansion to the SHL. The fluid velocity is calculated from (8).

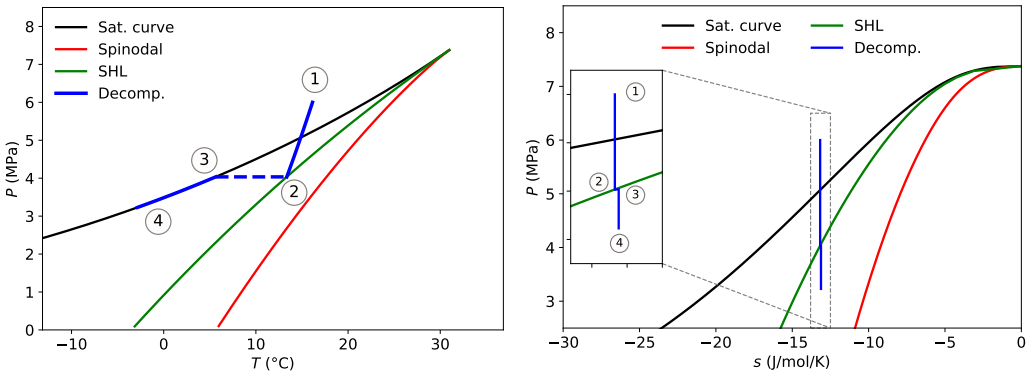

(a) Temperature-pressure space.

(b) Entropy-pressure space.

Figure 5: Expansion path (blue curve) illustrating the D-HEM. The path 1–2 is isentropic with no phase transfer, followed by the isenthalpic and isobaric path 2–3 where the metastable state 2 is transformed to the equilibrium two-phase state 3. If the flow is not critical, the expansion path ends in an isentropic two-phase equilibrium path 3–4. The saturation curve, liquid spinodal and SHL line are shown. All curves are calculated using the GERG-2008 EOS.

- Point 3 is the equilibrium state resulting from an isenthalpic evaporation process of the metastable liquid state at the SHL pressure.
- Point 4 is the isentropic HEM expansion from Point 3.

In the following we verify that D-HEM is physically sound, and does not violate the second law of thermodynamics. The overall enthalpy, H, differential is given as

$$\mathrm{d}H = T\,\mathrm{d}S + V\,\mathrm{d}P + \mu\,\mathrm{d}N. \tag{10}$$

Here, T is temperature, S is entropy, V is volume, μ is chemical potential and N is the number of moles. Setting the differential to zero, at constant pressure for a pure fluid distributed in two phases, we have,

$$\mathrm{d}H = \mathrm{d}\left(H_\mathrm{g} + H_\ell\right) = T_\mathrm{g}\,\mathrm{d}S_\mathrm{g} + T_\ell\,\mathrm{d}S_\ell + \mu_\mathrm{g}\,\mathrm{d}N_\mathrm{g} + \mu_\ell\,\mathrm{d}N_\ell = 0. \tag{11}$$

If we assume temperature equilibrium between the phases, we get $T_\mathrm{g}\,\mathrm{d}S_\mathrm{g} + T_\ell\,\mathrm{d}S_\ell = T\,\mathrm{d}\left(S_\mathrm{g} + S_\ell\right) = T\,\mathrm{d}S$.

For a process of bubble nucleation, we have $dN = \mathrm{d}N_\mathrm{g} = -\,\mathrm{d}N_\ell$, which gives the following entropy production for the phase transition,

$$\frac{dS}{dN} = \frac{\mu_\ell - \mu_\mathrm{g}}{T}. \tag{12}$$

As the liquid fugacity in the metastable region is higher than the gas fugacity, the phase transition will produce entropy. The effect of the entropy production in mass flux predictions is small, and could probably be ignored at the expense of having a discontinuous velocity at the SHL pressure. In this work we include the effect of entropy production.

Even if the fluid velocity is continuous at the SHL pressure, the density is not, giving a discontinuous reduction in mass flux during the isenthalpic evaporation. If the fluid reaches sonic velocities after the SHL, the choke flux is taken as the maximum of the flux at the SHL and the flux where the HEM chokes.

3.6. Flow contraction at orifices

The coefficient of contraction is defined as the ratio between the area of the jet at the vena contracta and the area of the restriction geometry,

$$C_{\mathrm{C}} = \frac{A_{\mathrm{vc}}}{A_{\mathrm{res}}}. \tag{13}$$

See also Figure C.14 in Appendix C. For a nozzle, the streamlines follow the geometry, except in a thin boundary layer, and the loss is very small. By using the method of Tesař (2008) we have estimated the contraction coefficient for our cases to be larger than $C_{\mathrm{C}} = 0.99$. For simplicity, we round off to $C_{\mathrm{C}} = 1$.

On the other hand, for a sharp-edged orifice, $C_{\mathrm{C}} < 1$. For an incompressible, ideal flow in a sharp-edged orifice, the contraction coefficient is known to be (Lienhard and Lienhard, 1984),

$$C_{\mathrm{C,i}} = \frac{\pi}{\pi + 2}. \tag{14}$$

By making a simple assumption about the flow pattern at the walls, Bragg (1960) accounted for the compressibility effects on the contraction coefficient. Using a force balance on the fluid from upstream of the flow restriction down to the vena contracta, he derived equations for the contraction coefficient of isentropic ideal gas flow. In this work we use the same assumptions but rigorously solve the GERG-2008 EOS for the properties of the flow. In the calculation of the contraction coefficient we assume frozen flow, i.e., no phase transfer. The incompressible contraction coefficient in (14) is used as input to the model of Bragg (1960). Further details on the calculation of the contraction coefficient can be found in Appendix C.

3.7. Pipe-flow model

We have implemented the quasi-steady-state HEM, D-HEM and HF models for flow through restrictions discussed above in our numerical workbench for 1D, transient, multiphase, multicomponent flow in pipes. In the inner domain of that model, the fluid flow is modelled using the HEM including source terms for wall friction and heat transfer through the pipe wall. The model has been presented previously (Munkejord and Hammer, 2015; Munkejord *et al.*, 2016), and we briefly review it here for completeness. We remark that it is common to use separate outflow models to provide the boundary conditions to transient pipe-flow models (see Elias and Lellouche, 1994, Sec. 4).

The governing equations have the same form as the Euler equations for single-phase, compressible, inviscid flow, and consist of a mass-conservation equation,

$$\frac{\partial}{\partial t}(\rho) + \frac{\partial}{\partial x}(\rho u) = 0, \tag{15}$$

a momentum-balance equation,

$$\frac{\partial}{\partial t}(\rho u) + \frac{\partial}{\partial x}(\rho u^2 + P) = -\mathcal{F}, \tag{16}$$

and a balance equation for the total energy,

$$\frac{\partial}{\partial t}(E) + \frac{\partial}{\partial x} u(E + P) = \mathcal{Q}. \tag{17}$$

Herein, $\rho = \alpha_g \rho_g + \alpha_\ell \rho_\ell$ is the density of the gas (g) and liquid (ℓ) mixture. u is the common velocity and P is the pressure. $E = \rho(e + 1/2u^2)$ is the total energy density of the mixture, while $e = \left(e_g \alpha_g \rho_g + e_\ell \alpha_\ell \rho_\ell\right)/\rho$ is the mixture specific internal energy. α_k denotes the volume fraction of phase $k \in \mathrm{g}, \ell$. $\mathcal{F}$ is the wall friction and $\mathcal{Q}$ is the heat transferred through the pipe wall to the fluid. The wall friction is calculated by the Friedel (1979) correlation. The heat conduction through the pipe steel and the surrounding insulation is calculated by solving the heat equation in the radial direction in a two-layer domain, as described by Aursand *et al.* (2017). The in-pipe heat-transfer coefficient is calculated based on the Dittus–Boelter correlation, see e.g. Bejan (1993, Chap. 6). The outside heat-transfer coefficient is estimated to be $4\,\mathrm{W/(m^2\,K)}$. For more details on the friction and heat-transfer modelling, see Munkejord *et al.* (2021).

At the outflow boundary, a flux, $\boldsymbol{F}$, is enforced for the governing equations (15)–(17). Given the mass flux per cell cross-sectional area,

$$j_{\mathrm{pipe}} = j_{\mathrm{res}} \frac{A_{\mathrm{res}}}{A_{\mathrm{pipe}}}, \tag{18}$$

calculated from the restricted-flow model, and the state of the boundary cell, the following flux vector is used,

$$\boldsymbol{F} = \begin{bmatrix} j_{\mathrm{pipe}} \\ j_{\mathrm{pipe}} u_{\mathrm{b}} + P_{\mathrm{b}} \\ j_{\mathrm{pipe}} \left(h_{\mathrm{b}} + \frac{1}{2} u_{\mathrm{b}}^2\right) \end{bmatrix}. \tag{19}$$

Here, the subscript b refers to the cell at the end of the inner pipe domain adjacent to the outflow restriction. In the case when $j_{\mathrm{pipe}} = (\rho u)_{\mathrm{b}}$, the flux will extract mass from the pipe isentropically. However, numerically, we see a small entropy production at the boundary.

We solve the system (15)–(17) using the finite-volume method, where the numerical fluxes are calculated using the first-order centred (FORCE) scheme (Toro and Billett, 2000). As described in Hammer *et al.* (2013), we obtain a second-order method by employing a semi-discrete monotone upwind-centred scheme for conservation laws (MUSCL) along with a second-order strong-stability-preserving Runge–Kutta method. For the simulations performed in this work, we employed a Courant–Friedrichs–Lewy (CFL) number of 0.85, and a spatial grid of 4800 cells. The Span–Wagner EOS is used to calculate the CO_2 fluid properties.

Table 2: Experimental conditions of the depressurization tests of CO_2 with orifices and nozzles.

Test no.	Type	Diameter (mm)	Aperture ratio (%)	Pressure avg. (MPa)	Temperature avg. (°C)	Ambient temp. (°C)	Figures
8**	Full-bore	40.8	100	12.22	24.6	9	6. 8b
13*	Orifice	12.7	9.7	12.75	24.6	12	6, 10a
16*	Orifice	4.5	1.2	12.18	24.7	7	6, 10c
17*	Nozzle	4.5	1.2	12.43	25.2	7	6, 9c
18*	Nozzle	12.7	9.7	12.41	25.4	9	6, 9a
20*	Nozzle	9.0	4.9	11.42	23.4	7	6, 9b
21*	Orifice	9.0	4.9	11.51	23.2	0	6, 10b

* Present work. ** Munkejord *et al.* (2020).

4. Results and discussion

In this section, we present new pipe-depressurization data taken at the same nominal conditions (12 MPa, 25 °C) for same-size nozzles and orifices. Next, we compare measured pressure traces with transient 1D CFD simulations and discuss the performance of the different restricted-flow models. Finally, we expand the analysis of the restricted-flow models by including published data on flow through nozzles.

4.1. Pipe depressurization

The initial conditions of the depressurization experiments and the restrictions are listed in Table 2. We report on six experiments with three sizes of orifices and nozzles. A previous full-bore experiment (Test 8) is included as a reference.

4.1.1. Pressure response to different outlet restrictions

Figure 6 shows the pressure measured at $x = 0.08$ m from the outlet in the seven tests 8, 13, 16, 17, 18, 20 and 21 defined in Table 2. Following a single pressure trace, e.g. Test 13, we observe that the pressure drops fast from the initial level to a plateau of 9.5 MPa upon arrival of the first rarefaction wave. The pressure remains at the plateau for about 0.3 s, the time required for the wave to travel to the closed end and be reflected back, after which the pressure again drops to a lower plateau value. When the wave enters the two-phase region, the evaporated gas will maintain the pipe pressure while the mass flux drops.

The effect of the outlet restriction sizes can be seen by comparing the full-bore test (no. 8) and the nozzle tests (nos. 17, 18 and 20) in Figure 6. One can observe that for the full-bore test, there is only one pressure plateau and it lasts for very short time. The pressure continues to drop afterwards and enters the two-phase region. For the tests with a restricted outlet, the number of pressure plateaux increases as the diameter decreases, and it takes longer to reach a two-phase state.

The difference between nozzles and orifices of the same diameter can also be observed in Figure 6. When comparing Tests 16 (orifice) and 17 (nozzle), fewer pressure plateaux are observed for the nozzle, and the pressure levels are lower.

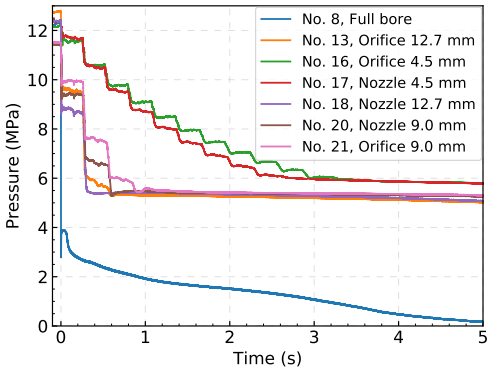

Figure 6: Measured pressure at $x = 0.08$ m for the tests in Table 2.

This is caused by the vena contracta area reduction of the orifice. In the end, both cases reach a similar two-phase pressure state.

4.1.2. Comparison of HEM and D-HEM

Before discussing results obtained using our transient pipe-flow model, we want to consider some of the differences between HEM and D-HEM presented in Section 3.5. Figure 7 compares HEM and D-HEM for a decompression process, plotting speed of sound and fluid velocity as a function of pressure for pure CO_2. The effect of the delayed phase transition is seen to be small for the fluid velocity, but the impact on the speed of sound is large, due to the difference in the equilibrium speed of sound compared to the metastable liquid speed of sound. The effect on fluid velocity of reducing the pressure along the same isentrope is also illustrated. For sufficiently low pressures, 5.5 MPa in the example, the flow will no longer choke at the SHL but in the following delayed HEM flow region.

We now consider two full-bore depressurization tests (Tests 6 and 8) reported in Munkejord *et al.* (2020). In Figure 8, we have plotted experimentally observed decompression-wave speeds along with model predictions by HEM and D-HEM. The modelled decompression-wave speed curves are found by integrating (1). Such curves are valuable for assessing running ductile fracture in pipelines, and are often plotted together with the fracture speed in the Battelle two-curve method (see Aursand *et al.*, 2016a). For Test 6, we observe in Figure 8a that the decompression path enters the two-phase region close to the critical pressure. In this case, the HEM and D-HEM have the same performance, and they are both in good agreement with the experiment. For Test 8, shown in Figure 8b, the decompression path enters the two-phase region at a lower pressure. Here, the HEM predicts phase transition at about 5.2 MPa, whereas the D-HEM gives phase transition at about 4.2 MPa. This level agrees well with the experiment, which indicates departure from thermodynamic equilibrium in the flow path. However, in the experiment, we observe a more gradual transition between a metastable state and a more homogeneous equilibrium state, indicating less entropy production than calculated by the D-HEM.

The difference between Tests 6 and 8 can be further illuminated by considering

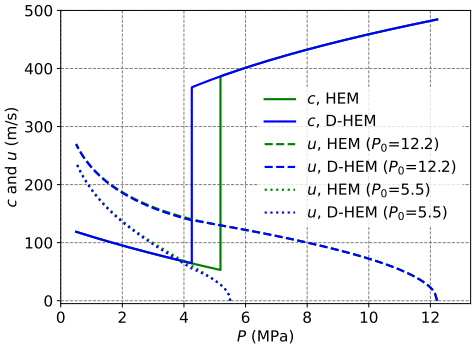

Figure 7: Comparison of D-HEM and HEM for a decompression process. Speed of sound (full lines) and fluid velocity (dashed and dotted lines) as a function of pressure. The initial state of Test 8 (12.2 MPa, 24.6 °C) defines the stagnant state for the dashed lines, whereas that of the dotted lines is (5.5 MPa,16.3 °C), on the same isentrope. The GERG-2008 EOS is used for the property predictions. The fluid velocity curves for the different models are very similar and might be difficult to distinguish.

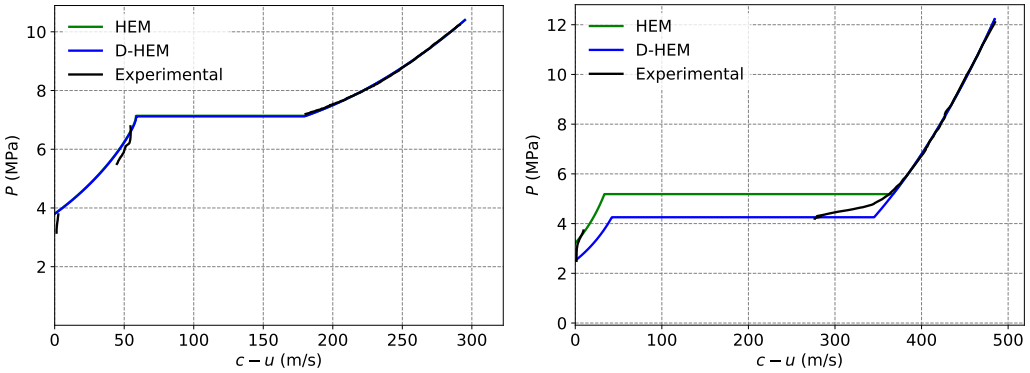

(a) Test 6: $T_0 = 39.5\,^{\circ}\mathrm{C}$, $P_0 = 10.4\,\mathrm{MPa}$.

(b) Test 8: $T_0 = 24.6\,^{\circ}\mathrm{C}$, $P_0 = 12.22\,\mathrm{MPa}$.

Figure 8: Experimentally observed and calculated decompression-wave velocities for full-bore depressurizations of pure CO_2 (Munkejord *et al.*, 2020, Figs. 14 and 15). The GERG-2008 EOS is used for the property predictions.

Figure 5a. Close the critical point, there is little difference between the superheat limit and the saturation curve. Therefore, for Test 6, there is little difference between HEM and D-HEM, as opposed to the case for Test 8.

4.1.3. Comparison of nozzle experiments and 1D CFD simulations

We have simulated the above cases employing our transient pipe-flow model described in Section 3.7 together with the restricted-flow models in Section 3.4. Figure 9 displays the measured and simulated pressure for Tests 17, 18 and 20 with nozzles, at $x = 0.08\,\mathrm{m}$ from the outlet.

In Figure 9a for Test 18 with a 12.7 mm nozzle, we observe a fast pressure drop

to a plateau pressure of 8.8 MPa, and the plateau remains for about 0.26 s. Upon arrival of the decompression wave reflected from the closed end of the pipe, the pressure further decreases. As already shown in Figure 6, there are several plateaux before the two-phase region is reached. The pressures simulated using the three restricted-flow models, HEM, HF, and D-HEM, are similar and agree well with the measurements. The HEM predicts the highest pressure plateau (about 8.9 MPa) and smallest mass outflow rate while the D-HEM predicts the lowest pressure plateau (about 8.6 MPa) and largest mass outflow rate. The HEM tends to overestimate the plateau pressure due to the underestimation of mass outflow rate. In the present case, the HF model appears to match the measurement best.

Figure 9b shows the results for Test 20 with a 9.0 mm nozzle. The experimentally observed pressure plateau is increased to about 9.4 MPa, otherwise the trends are very similar to those in Figure 9a.

In Figure 9c for Test 17 with a 4.5 mm nozzle, the simulated pressure plateau matches well with the measured values for the first 0.06 s. Later, the measured pressure is affected by pressure waves present in the pipe before the disk rupture. Since the pressure drop is smaller for a smaller-diameter nozzle, the disturbance is relatively more significant in this case.

In Figures 9a, 9b and 9c, we observe a small intermediate pressure plateau between the initial pressure and the main plateau. This is related to the gradual opening of the triple-layer rupture disk. The effect is most pronounced for the small-diameter nozzle, most likely due to the smaller flow rate. To account for the reduced flow area in Tests 17 and 20, the mass flux at the intermediate plateau is calculated using (1), and an area scaling is calculated as the fraction of the intermediate mass flux and the main plateau mass flux. For Test 17, a reduced area fraction of 0.371 is applied for the initial 9.8 ms of the simulation. For Test 20, a reduced area fraction of 0.295 is applied for the initial 6.7 ms of the simulation. For Test 18, the effect of the gradual opening is ignored.

4.1.4. Comparison of orifice experiments and 1D CFD simulations

For the simulations of the tests with orifices, we employ contraction coefficients as described in Section 3.6. The employed coefficients are given in Table 4. In addition, for Test 16, a reduced area fraction of 0.43 is applied for the initial 18.09 ms. For Test 21, a reduced area fraction of 0.35 is applied for the initial 7.51 ms. Test 13 was conducted using a single-layer rupture disk not prone to the gradual opening of the triple-layer disks.

Figure 10a shows the measured and calculated pressure for Test 13 with a 12.7 mm orifice. In this case, the calculated contraction coefficient, C_C, has a value of 0.75. It can be seen that all the three restricted-flow models show good agreement with the measured pressure. The HF model matches the measurement best, while the HEM predicts a slightly higher pressure plateau and the D-HEM predicts a slightly lower one. As can be seen in Figure 10b, the trends are similar for Test 21 with a 9.0 mm orifice.

In Figure 10c, we compare the measured and simulated pressure for Test 16 with a 4.5 mm orifice. In this case, the procedure in Section 3.6 to estimate the contraction coefficient, C_C, yields a value of 0.74. One can see that all the models overestimate the plateau pressure, and that the HF and D-HEM give almost the same results.

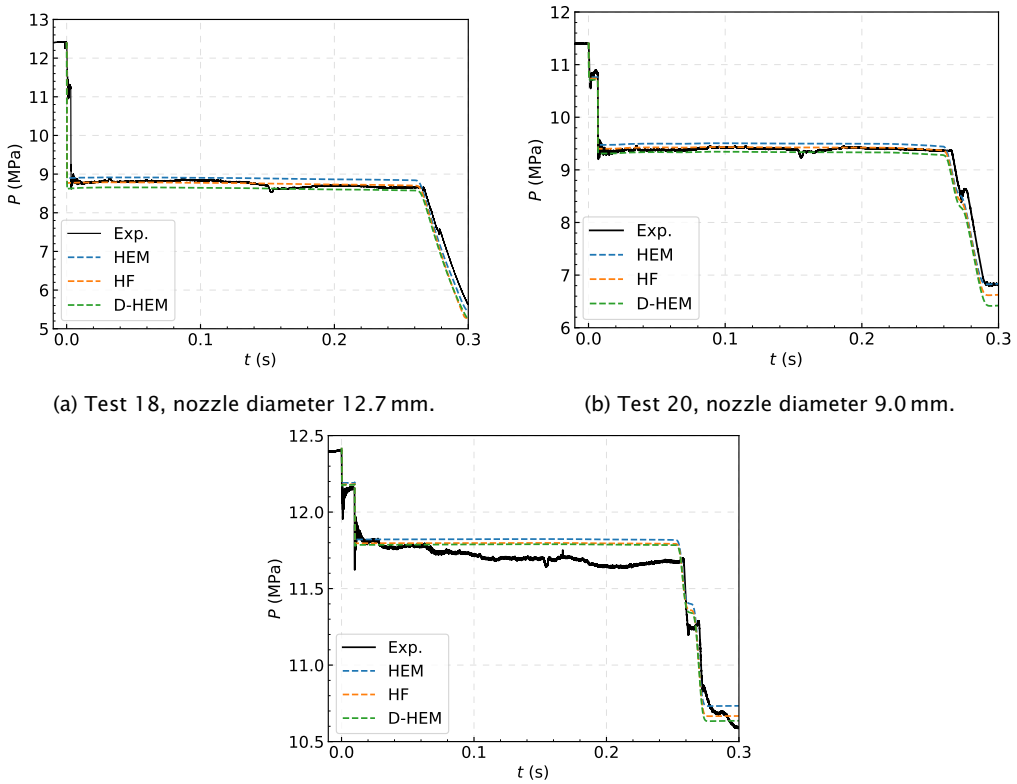

(a) Test 18, nozzle diameter 12.7 mm.

(b) Test 20, nozzle diameter 9.0 mm.

(c) Test 17, nozzle diameter 4.5 mm.

Figure 9: Measured (full lines) and simulated pressure (dashed lines) at $x = 0.08$ m for Tests 18, 20 and 17 with nozzles.

4.1.5. Analysis of restricted-flow models

We will now further analyse the models presented in Section 3.4. In doing so, we consider the pressure jump in the decompression (rarefaction) wave between the initial pressure and the first pressure plateau. The flow resulting from this pressure drop is regarded as steady. The initial temperature and pressure at the outlet, as well as the observed pressure-plateau value are given in Table 3. (The values given in Table 2 are averages for the whole pipe.) Using the GERG-2008 EOS and the Euler compatibility equation (1), we calculate the mass flow rate in the pipe integrating (2) isentropically using an adaptive Gauss–Legendre quadrature, and convert it to an equivalent mass flux through the nozzle or orifice. This will be used as the experimental value in the following discussion. Further details on the calculation of the mass flow rate and the experimental uncertainty are given in Appendix D.

In order to illustrate the state where the flow chokes in the orifice or nozzle at the outlet, Figure 11 shows the isentropic path from the pressure plateau after the first decompression wave down into the metastable region for frozen flow. The initial state is given by the plateau pressure and the initial entropy (P_1, s_0). The isentrope

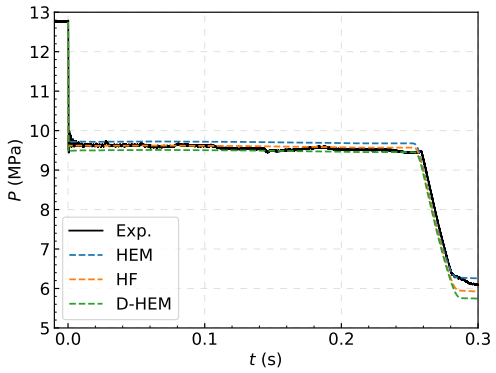

(a) Test 13, orifice diameter 12.7 mm, contraction coefficient $C_C = 0.75$.

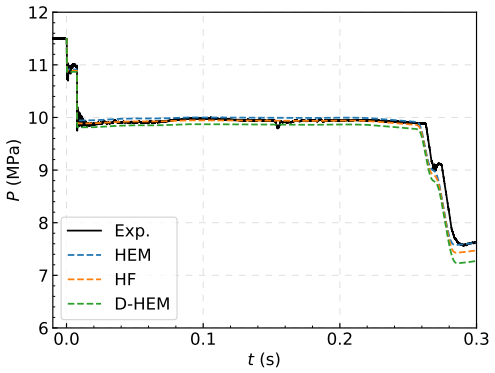

(b) Test 21, orifice diameter 9.0 mm, contraction coefficient $C_C = 0.74$.

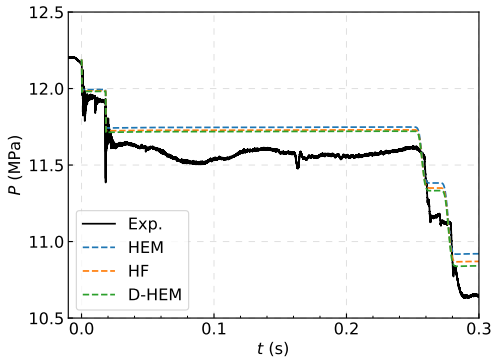

(c) Test 16, orifice diameter 4.5 mm, contraction coefficient $C_C = 0.74$.

Figure 10: Measured (full lines) and simulated pressure (dashed lines) at $x = 0.08$ m For Tests 13, 21 and 16 with orifices.

Table 3: Mass flow estimated from experimental pressure drop using the $x = 0.08$ m sensor. The mass flux is $j = \dot{m}/A_{\text{res}}$.

Test no.	T_0 (°C)	P_0 (MPa)	P_1 (MPa)	$\dot{m}$ (kg/s)	j (t/(s m^2))
13 (orifice)	24.6	12.77	9.61	8.592	67.8
16 (orifice)	24.4	12.17	11.58	1.600	100.6
17 (nozzle)	25.2	12.40	11.74	1.807	113.6
18 (nozzle)	25.1	12.41	8.81	10.072	79.5
20 (nozzle)	22.7	11.40	9.40	5.515	86.7
21 (orifice)	22.0	11.50	9.94	4.208	66.2

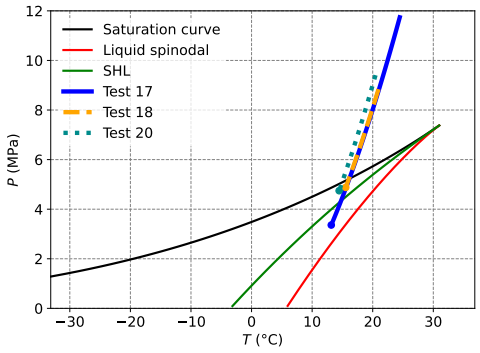

Figure 11: Restricted-flow calculation for Tests 17, 18 and 20: Isentropic path assuming frozen flow. The choke point (dot) calculated from observed mass flux for each experiment. GERG-2008 spinodal and superheat limit calculated from CNT are included.

is mapped down to the pressure where the single-phase (stable or metastable) flux, calculated using (8) and the local density, equals the flux calculated across the decompression wave and given in Table 3. For the two largest nozzles, Test 18 and 20, the process ends at a pressure between the saturation curve and the SHL curve. This indicates that the process departs from thermodynamic equilibrium.

For Test 17, however, the flow predicted to choke below the SHL curve, which is lower than expected. The most likely explanation for this result is the uncertainty in the calculated flow rate, due to the small pressure difference between P_0 and P_1. As little as a 0.035 MPa increase in P_1 is enough for Test 17 to terminate at the SHL.

For the orifice geometry, the contraction coefficient is calculated using the method outlined in Section 3.6, and it is listed along with the mass fluxes predicted using the HEM, D-HEM and HF models in Table 4. The relative deviation to the experimental values are shown in parenthesis.

As the flow apparently chokes below the SHL curve for Test 17, D-HEM agrees best with that experiment, with an underprediction of the mass flux of 5 %. For the largest nozzles, Test 18 and 20, the HF model gives the best prediction of the mass flux, with an overprediction of 1 %. D-HEM overpredicts by 6 % for Test 18 and 7 % for Test 20, while HEM underpredicts by 4 % and 3 %, respectively.

For the small orifice (Test 16), the predicted mass fluxes are off by more than −20 % for all models. For the largest orifice, the HF model gives the best result, only underpredicting the mass flux by 1 %. For the medium orifice (Test 21), the HEM model agrees well with the experimental flux (less than 0.5 % deviation), while the HF and the D-HEM model overpredict the flux by 5 % and 10 %, respectively.

4.2. Mass flux through a nozzle

We now consider the mass flux of dense-phase CO_2 through a converging-diverging nozzle, using the data of Banasiak and Hafner (2013) as reference. Figure 12 shows a comparison between the experimental data and values calculated using the HEM, D-HEM and HF models. The experimental data are taken at different temperatures and pressures, and are not straightforward to plot two-dimensionally. To

Table 4: Calculated contraction coefficient and predicted mass flux (tonnes per square metre and second). Relative deviation to experimental data in parenthesis.

Test no.	C_C (-)	j_{HEM} (t/(s m^2))	$j_{D\text{-}HEM}$ (t/(s m^2))	j_{HF} (t/(s m^2))
13 (orifice)	0.75	63.9 (–6 %)	70.1 (3 %)	66.8 (–1 %)
16 (orifice)	0.74	74.8 (–26 %)	79.6 (–21 %)	78.1(–22 %)
17 (nozzle)	1.0	101.6 (–11 %)	107.7 (–5 %)	106.1 (–7 %)
18 (nozzle)	1.0	76.1 (–4 %)	84.5 (6 %)	80.3 (1 %)
20 (nozzle)	1.0	83.7 (–3 %)	92.5 (7 %)	87.6 (1 %)
21 (orifice)	0.74	66.4 (0 %)	73.0 (10 %)	69.3 (5 %)

Table 5: Relative absolute errors for model predictions compared to Banasiak and Hafner (2013) experimental data.

Model	Rel. Abs. Err. (All data) (%)	Rel. Abs. Err. (Low press data) (%)
HEM	7.8	17
D-HEM	2.5	5.8
HF	5.4	8.2

get most of the information into one graph, we have plotted mass flux indirectly against the inlet entropy. The x-axis variable is calculated as the saturation pressure corresponding to the stagnant inlet entropy, $P = P_{sat}\,(s\,(T_0, P_0))$. Banasiak and Hafner estimated the experimental uncertainty to be ±0.5 K for the inlet temperature, ±30 kPa for the pressure and $\pm 0.5\times10^3$ kg/s for the mass flow rate. With these estimates, error bars have been calculated for the saturation pressure and the mass flux. In Figure 12, the dashed line separates data with an inlet pressure above or below 8.2 MPa.

We observe that the HF model is in good agreement with the experimental data, with the exception of some points with low inlet pressure and low inlet entropy where the mass flux is underpredicted. The HEM is seen to predict the mass flux well for entropies close to the critical point. However, elsewhere, the model underpredicts the mass flux. This is expected because the distance between the saturation curve and the SHL is small in this region, and the delay before onset of nucleation is short. The D-HEM is in very good agreement with the experimental data points above the grey dashed line. From Table 5 we see that D-HEM outperforms HF both for the low-pressure data and when all data are taken into account. For the latter case the mean absolute deviation is 2.5 % for D-HEM versus 5.4 % for HF.

Finally, we consider the experimental data of Hesson and Peck (1958) for saturated liquid flowing through a converging nozzle. Figure 13 shows a comparison between the experimentally determined mass-flux data and values calculated using the HEM, D-HEM and HF models, plotted as a function of the reported saturation pressure of the experiments. Both HEM and D-HEM are seen to consistently underpredict the data. With the exception of the data point with the lowest saturation pressure, HEM and D-HEM give almost the same result, the only difference being the small entropy production in D-HEM. For the experiment starting at 5.25 MPa, D-HEM predicts

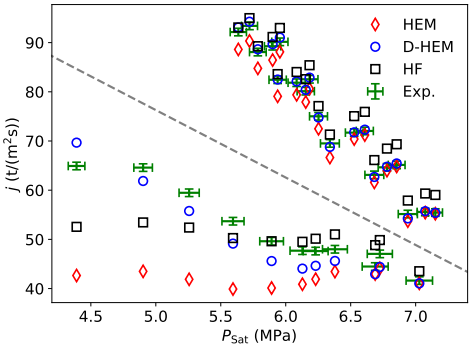

Figure 12: Model predictions using HF, HEM and D-HEM, plotted together with the Banasiak and Hafner (2013) experimental data (Exp.). The experimental data include error bars calculated using the uncertainties reported by Banasiak and Hafner. The mass flux is plotted as a function of the saturation pressure calculated from the stagnant inlet conditions, $P = P_{\mathrm{sat}}\left(s\left(T_0, P_0\right)\right)$. The GERG-2008 EOS is used for the property predictions. The dashed grey line separates data based on inlet pressure, below it, all data have an inlet pressure below 8.2 MPa.

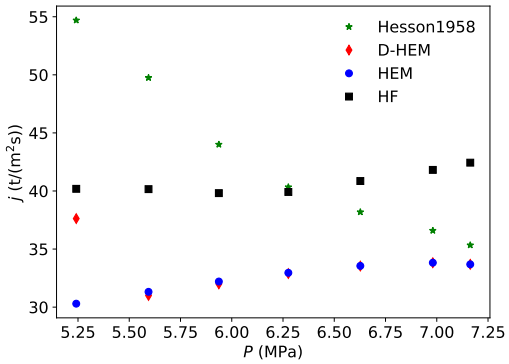

Figure 13: Model predictions using HF, HEM and D-HEM, plotted together with the Hesson and Peck (1958) experimental data for saturated liquid states. The GERG-2008 EOS is used for the property predictions.

choking before the SHL line, leading to a larger mass flux than for HEM. For the other points, D-HEM chokes after the SHL and the mass flux is slightly lower than for HEM due to the entropy production.

The HF model overpredicts the mass flux close to the critical pressure. However, for saturation pressures below 6.25 MPa, it underpredicts the experimental mass flux. As reported by Hendricks *et al.* (1972), the mass fluxes in Hesson and Peck (1958) are higher than expected and there might be systematic errors in the data.

5. Conclusion

In CO_2 processing, transportation and injection systems, compressed CO_2 will, during normal operation or exceptional venting, flow through valves or other restrictions. In order to calculate the flow rates and fluid states needed for operational or safety considerations, there is a need for validated models providing realistic results without the need for detailed geometry input.

We have experimentally investigated the effect of outlet restriction geometry type and size on the depressurization of a 41 mm inner-diameter pipe. From an initial state of 12 MPa and 25 °C, the pipe was depressurized through six sharp orifices and converging nozzles, made in pairs with 90 %, 95 % and 99 % area reduction.

In our previous full-bore experiment, the pressure in the pipe rapidly decreased to a two-phase state. The introduction in this work of flow restrictions at the outlet yielded pressure traces displaying intermediate plateaux at single-phase states, the number of plateaux and time to empty the pipe increasing for decreasing restriction diameter. For a given diameter, flow through an orifice yielded higher pressure-plateau levels than for flow through a nozzle. This is consistent with the orifice resulting in a smaller practical cross-sectional area (vena contracta), which in turn gives a smaller mass flow rate.

Our current setup does not allow the direct measurement of the mass flow rate. However, by exploiting the fact that the state in the pipe was single-phase, and by assuming a quasi-steady state for each pressure plateau, we could calculate the mass flow rate based on the measured pressure. Here, we employed the Euler compatibility equation, which is commonly used for hydraulic-shock calculations, and the GERG-2008 EOS.

Three different models were used to calculate the flow through the restrictions. All the models were formulated in a manner not requiring integration over the actual geometry, but only using the upstream state and the minimum cross section of the restriction. The models are therefore valid when the influence by friction on the flow rate can be assumed to be small. This is useful in simulations where the spatial dimension of the restriction is not resolved (long pipes) or for cases where the geometry is partly unknown.

In addition to the classical HEM and HF model, we propose an augmented HEM, allowing for delayed phase transition, labelled D-HEM. The model assumes a process where there are no bubble nuclei before reaching the SHL calculated by classical nucleation theory. After reaching the SHL, the state is transitioned to full equilibrium at constant pressure, including entropy production during phase transfer.

We compared the three models to experimental data for flow through nozzles by Hesson and Peck (1958) and Banasiak and Hafner (2013). The mass fluxes reported by Hesson and Peck are significantly larger than those predicted by the models. This is an inconsistency that has also been noted by other authors. For the Banasiak and Hafner experiments we found the D-HEM to be the best model among those tested, with a relative absolute error of 2.5 % for the predicted mass flux. This indicates that the approach behind D-HEM is viable and should be considered in the further development of simulation tools for compressed CO_2.

Another promising avenue for further research is to apply the D-HEM in the assessment of running ductile fracture in CO_2-transportation pipelines. We gave ex-

amples of typical plots of pressure as a function of decompression-wave speed used in such assessments, showing that D-HEM is applicable and gives lower pressures than HEM, which is known to give too high pressures and therefore the wrong load on the steel structure.

In the sharp-orifice geometry, the actual flow throat area will be smaller than the minimum physical area. We accounted for this by calculating a contraction coefficient employing a steady-state force balance, an approach generalized from that of Bragg (1960).

The above models for flow through restrictions were implemented in our numerical workbench for 1D, transient, multiphase flow, and we compared simulated and measured pressures. Good results were obtained for all models, with the best agreement obtained using the HF model. For the pressure-plateau, the HEM gave the highest level, consistent with the lowest mass flow rate, followed by the HF model and D-HEM. Our results for the decompression through orifices indicate that the calculated contraction coefficient is uncertain. Further experimental and modelling efforts are needed here.

A subject for future work would be to study cases with different initial fluid states, so that the isentropic decompression path hits the two-phase region at a low pressure and temperature, where heterogeneous nucleation needs to be accounted for.

Another topic for further work would be to modify the experimental setup and procedure in order to have a more uniform initial condition.

Acknowledgements

This publication has been produced with support from the NCCS Centre, performed under the Norwegian research programme Centres for Environment-friendly Energy Research (FME). The authors acknowledge the following partners for their contributions: Aker Carbon Capture, Allton, Ansaldo Energia, Baker Hughes, CoorsTek Membrane Sciences, Equinor, Fortum Oslo Varme, Gassco, Krohne, Larvik Shipping, Lundin Energy Norway, Norcem, Norwegian Oil and Gas, Quad Geometrics, Stratum Reservoir, TotalEnergies, Vår Energi, Wintershall Dea and the Research Council of Norway (257579).

The construction of the ECCSEL Depressurization Facility was supported by the INFRASTRUKTUR programme of the Research Council of Norway (225868).

Appendix A. Experimental data

The experimental data used in this study are attached as a supplementary file.

Appendix B. Calculation of choking conditions for steady-state HEM

This section outlines the calculation of the choking condition of the HEM model under a steady-state assumption. The case of the HF model is given in the original article (Henry and Fauske, 1971). How to solve the D-HEM model is indicated in Section 3.5.

In steady state, the HEM without source terms reduces to three flow constants:

- constant mass flow rate: $\dot{m}$,
- constant entropy: s,
- constant energy: $h + \frac{1}{2}u^2$.

The energy equation, subject to constant entropy, will give $u = u(p)$. Under the same conditions, the speed of sound will be a function of pressure, $c = c(p)$, and solving for $u = c$ is a single-variable problem in pressure. One complication is the discontinuity in speed of sound at the phase boundaries. This is seen in Figure 7 where u and c are plotted as functions of p for one test condition. Due to the discontinuity, the flow will often choke on the saturation curve.

The speed of sound is given by

$$c = \sqrt{\frac{\partial p}{\partial \rho}\bigg|_s}. \tag{B.1}$$

Under the HEM assumption of chemical equilibrium ($\mu_g = \mu_\ell$), this equation becomes constrained. This can be accounted for by defining the following equation system where entropy (s_{cons}) and mass density (ρ_{cons}) are known,

$$\boldsymbol{G}\left(s_{\text{cons}}, \rho_{\text{cons}}, \boldsymbol{X}\right) = \boldsymbol{0}, \tag{B.2}$$

where

$$\boldsymbol{G} = \begin{bmatrix} \mu_g - \mu_\ell \\ \dfrac{1}{\frac{z}{\rho_g} + \frac{1-z}{\rho_\ell}} - \rho_{\text{cons}} \\ s - s_{\text{cons}} \end{bmatrix} \tag{B.3}$$

and

$$\boldsymbol{X} = \begin{bmatrix} T \\ P \\ z \end{bmatrix}, \tag{B.4}$$

with the overall entropy given as $s = z s_g + (1 - z) s_\ell$.

Differentiating the equation (B.2) with respect to ρ_{cons} we get

$$\nabla_{\boldsymbol{X}} \boldsymbol{G} \frac{\partial \boldsymbol{X}}{\partial \rho_{\text{cons}}} + \frac{\partial \boldsymbol{G}}{\partial \boldsymbol{\rho}_{\text{cons}}} = \boldsymbol{0}, \tag{B.5}$$

where $\nabla_{\boldsymbol{X}} \boldsymbol{G}$ is the Jacobian matrix of $\boldsymbol{G}$ with respect to $\boldsymbol{X}$ and $\partial \boldsymbol{G}/\partial \rho_{\text{cons}} = [0, -1, 0]^\intercal$. Solving for $\partial \boldsymbol{X}/\rho_{\text{cons}} = [\partial T/\partial \rho_{\text{cons}}, \partial P/\partial \rho_{\text{cons}}, \partial z/\partial \rho_{\text{cons}}]^\intercal$, we obtain $\partial P/\partial \rho$, and the speed of sound can be calculated. The speed of sound is calculated using an analytical Jacobian matrix and the discontinuity when entering the two-phase region is illustrated in Figure 7.

Appendix C. Calculation of the flow contraction coefficient at orifices

The coefficient of contraction, defined in Section 3.6, establishes the actual flow area and must be known when calculating the outflow through a nozzle or orifice. In

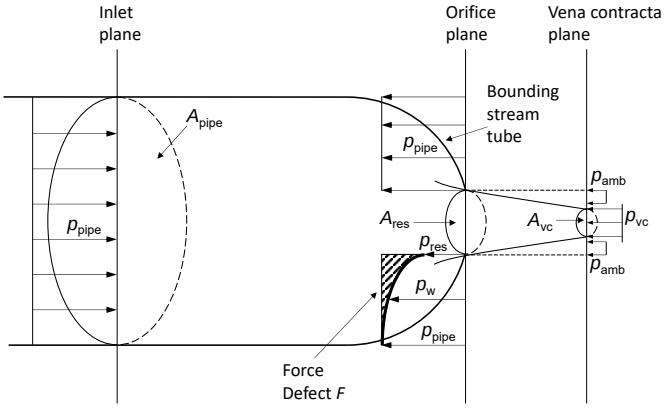

Figure C.14: Generalized orifice flow with notation and forces on the fluid, adapted from Benedict (1971).

this work we have utilized an isentropic force balance as described by Bragg (1960, Eq. (5)) and Benedict (1971, Eq. (2)). The area and the forces acting on the fluid are illustrated in Figure C.14.

The force balance accounting for inlet momentum and back pressure is

$$F + A_{\text{pipe}} p_{\text{pipe}} - (A_{\text{pipe}} - A_{\text{res}})\, p_{\text{pipe}} = A_{\text{vc}} p_{\text{vc}} + (A_{\text{res}} - A_{\text{vc}})\, p_{\text{amb}} + \dot{m}\,(u_{\text{vc}} - u_{\text{pipe}})\,, \tag{C.1}$$

where F is the force defect described by the integral

$$F = \int_{A_{\text{res}}}^{A_{\text{pipe}}} (p_{\text{pipe}} - p_w)\, \mathrm{d}A_w, \tag{C.2}$$

where the subscript w refers to the wall, and F can be integrated using a Gauss–Legendre quadrature with error control. Dividing (C.1) by A_{res}, and setting $F^* = F/A_{\text{res}}$ we get,

$$F^* + p_{\text{pipe}} - p_{\text{amb}} + (p_{\text{vc}} - p_{\text{amb}})\, C_{\text{C}} = C_{\text{C}} \rho_{\text{vc}} u_{\text{vc}}\,(u_{\text{vc}} - u_{\text{pipe}})\,, \tag{C.3}$$

which yields

$$C_{\text{C}} = \frac{F^* + p_{\text{pipe}} - p_{\text{amb}}}{p_{\text{vc}} - p_{\text{amb}} + \rho_{\text{vc}} u_{\text{vc}}\,(u_{\text{vc}} - u_{\text{pipe}})}. \tag{C.4}$$

Bragg (1960, Eq. (15)) proposed that the mass velocity distribution on the stream tube boundary upstream of the orifice could be described as

$$j_w = k C_{\text{C}} j_{\text{vc}} A_{\text{res}} / A_w, \tag{C.5}$$

where

$$k = \sqrt{\frac{2}{C_{\text{C,i}}} - \frac{1}{C_{\text{C,i}}^2}}, \tag{C.6}$$

and

$$C_{\text{C,i}} = \frac{\pi}{\pi + 2}. \tag{C.7}$$

p_w can then be found implicitly by solving

$$j_w = \rho\left(s_{\text{pipe}}, p_w\right) u\left(s_{\text{pipe}}, p_w\right), \tag{C.8}$$

where the steady-state energy equation (Bernoulli) for isentropic flow is used to determine the velocity u_w:

$$h_{\text{pipe}} + \frac{1}{2}u_{\text{pipe}}^2 = h_w\left(s_{\text{pipe}}, p_w\right) + \frac{1}{2}u_w^2. \tag{C.9}$$

We use a bracketing solver to solve the equation (C.8).
To solve for the contraction coefficient we use a successive substitution approach as follows.

- Guess $C_{\text{C}} = 1.1 C_{\text{C,i}}$
- Set $C_{\text{C,old}} = 1$
- Calculate critical state based on upstream conditions. Output: p_{vc}, u_{vc}, ρ_{vc}
- Iterate until $\|C_{\text{C}} - C_{\text{C,old}}\| / C_{\text{C}} < 10^{-10}$:
  - Set $C_{\text{C,old}} = C_{\text{C}}$
  - Find F^* by integrating (C.2)
  - Calculate C_{C} from (C.4)

Appendix D. Experimental uncertainty of mass flow rate

The mass flow is calculated as

$$\dot{m} = (u\rho)_{P_1} A_{\text{Pipe}} \tag{D.1}$$

with

$$u(P) = \int_{P=P_0}^{P=P_1} \frac{\mathrm{d}P}{\rho c}. \tag{D.2}$$

The pressure measured at the position closest to the outlet, at $x = 0.08\,\text{m}$, by the sensor PT201 is used to determine the initial pressure, P_0, and first pressure plateau, P_1. The temperature measured at the position $x = 1.6\,\text{m}$ is used for T_0.

The value of P_1 is obtained by averaging the measurement between the time when the pressure plateau stabilizes and the time when a dip reaches about the middle of the pressure plateau, as indicated in Figure D.15. This dip is a result of the recoil of the pipe: When depressurization occurs, a wave travels in both the fluid and the stainless-steel pipe towards the closed end. The wave travelling in the steel has a speed of about $5800\,\text{m/s}$. After it reaches the end, the wave is reflected and travels back in the fluid, as seen by the dip.

The values of P_0 and T_0 are stable, thus we focus on the measurement uncertainty caused by the value of P_1. We employ the min-max method to estimate the uncertainty of the mass flow rate $\dot{m}$. The values of P_0, T_0, and P_1 are listed in Table D.6,

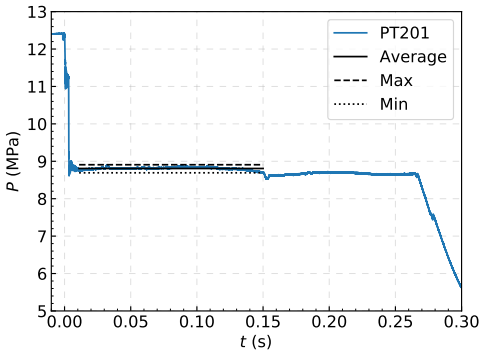

Figure D.15: Averaged plateau pressure P_1 for the calculation of mass flow rate in Test 18.

Table D.6: Initial pressure P_0, temperature T_0, and pressure plateau P_1 with differences to the maximum and minimum values.

Test no.	T_0 (°C)	P_0 (MPa)	P_1 (MPa)	$\delta P_{1,\max}$ (MPa)	$\delta P_{1,\min}$ (MPa)
13	24.6	12.77	9.61	0.14	0.09
16	24.4	12.17	11.58	0.07	0.07
17	25.2	12.40	11.74	0.09	0.06
18	25.1	12.41	8.81	0.10	0.12
20	22.7	11.40	9.40	0.06	0.10
21	22.0	11.50	9.94	0.06	0.10

with the differences to the maximum and minimum values $\delta P_{1,\max} = P_{1,\max} - P_1$ and $\delta P_{1,\min} = P_1 - P_{1,\min}$.

The mass flow rate for the maximum and minimum values of the pressure plateau can be expressed as

$$\dot{m}_{\min} = u\left(P_0, P_1 + \delta P_{1,\max}\right) \rho\left(P_0, P_1 + \delta P_{1,\max}\right) A_{\text{Pipe}}, \tag{D.3}$$

$$\dot{m}_{\max} = u\left(P_0, P_1 - \delta P_{1,\min}\right) \rho\left(P_0, P_1 - \delta P_{1,\min}\right) A_{\text{Pipe}}. \tag{D.4}$$

The measured mass flow rate can be expressed with the absolute uncertainty, $\dot{m} \pm \delta\dot{m}$, as

$$\delta\dot{m} = \max\left(\dot{m}_{\max} - \dot{m}, \dot{m} - \dot{m}_{\min}\right). \tag{D.5}$$

Since the data are not normally distributed, we use the maximum difference to $\dot{m}$ to be conservative. The relative uncertainty can be then expressed as $\frac{\delta\dot{m}}{\dot{m}}$. The absolute and relative uncertainties of the mass flow rates are listed in Table D.7.

References

Angielczyk, W., Bartosiewicz, Y., Butrymowicz, D., 2020. Development of delayed equilibrium model for CO_2 convergent-divergent nozzle transonic flashing flow. *Int. J. Multiphase Flow* 131, 103351. doi:10.1016/j.ijmultiphaseflow.2020.103351.

Table D.7: Measured mass flow rate and the absolute and relative uncertainties.

Test no.	$\dot{m}$ (kg/s)	$\dot{m}_{\max}$ (kg/s)	$\dot{m}_{\min}$ (kg/s)	$\delta\dot{m}$ (kg/s)	$\frac{\delta\dot{m}}{\dot{m}}$ (%)
13	8.592	8.850	8.203	0.389	4.5
16	1.600	1.799	1.400	0.201	12.5
17	1.807	1.972	1.567	0.241	13.3
18	10.072	10.408	9.781	0.336	3.3
20	5.515	5.788	5.339	0.273	4.9
21	4.208	4.489	4.037	0.280	6.7

Angielczyk, W., Bartosiewicz, Y., Butrymowicz, D., Seynhaeve, J.-M., Jul. 2010. 1-D modeling of supersonic carbon dioxide two-phase flow through ejector motive nozzle. In: *International Refrigeration and Air Conditioning Conference*. Purdue University. URL https://docs.lib.purdue.edu/iracc/1102/.

Angielczyk, W., Seynhaeve, J. M., Gagan, J., Bartosiewicz, Y., Butrymowicz, D., 2019. Prediction of critical mass rate of flashing carbon dioxide flow in convergent-divergent nozzle. *Chem. Eng. Process. – Process Intensif.* 143 (4), 107599. doi:10.1016/j.cep.2019.107599.

Armstrong, K., Allason, D., Oct. 2014. *2" NB shocktube releases of dense phase CO_2*. Tech. rep., GL Noble Denton, Gilsland Cumbria, UK. Available from https://www.dnvgl.com/oilgas/innovation-development/joint-industry-projects/co2pipetrans.html.

Aursand, E., Dumoulin, S., Hammer, M., Lange, H. I., Morin, A., Munkejord, S. T., Nordhagen, H. O., Sep. 2016a. Fracture propagation control in CO_2 pipelines: Validation of a coupled fluid-structure model. *Eng. Struct.* 123, 192–212. doi:10.1016/j.engstruct.2016.05.012.

Aursand, E., Hammer, M., 2018. Predicting triggering and consequence of delayed LNG RPT. *J. Loss Prevent. Proc.* 55, 124–133. doi:10.1016/j.jlp.2018.06.001.

Aursand, P., Gjennestad, M. A., Aursand, E., Hammer, M., Wilhelmsen, Ø., 2016b. The spinodal of single- and multi-component fluids and its role in the development of modern equations of state. *Fluid Phase Equilib.* 436, 98–112. doi:10.1016/j.fluid.2016.12.018.

Aursand, P., Hammer, M., Lavrov, A., Lund, H., Munkejord, S. T., Torsæter, M., Jul. 2017. Well integrity for CO_2 injection from ships: Simulation of the effect of flow and material parameters on thermal stresses. *Int. J. Greenh. Gas Con.* 62, 130–141. doi:10.1016/j.ijggc.2017.04.007.

Banasiak, K., Hafner, A., 2013. Mathematical modelling of supersonic two-phase R744 flows through converging–diverging nozzles: The effects of phase transition models. *Appl. Therm. Eng.* 51 (1), 635–643. ISSN 1359-4311. doi:10.1016/j.applthermaleng.2012.10.005.

Bejan, A., 1993. *Heat Transfer*. John Wiley & Sons, Inc., New York. ISBN 0-471-50290-1.

Benedict, R. P., 06 1971. Generalized contraction coefficient of an orifice for subsonic and supercritical flows. *J. Basic Eng.* 93 (2), 99–120. doi:10.1115/1.3425245.

Blinkov, V. N., Jones, O. C., Nigmatulin, B. I., 1993. Nucleation and flashing in nozzles – 2. Comparison with experiments using a five-equation model for vapor void development. *Int. J. Multiphase Flow* 19 (6), 965–986. doi:10.1016/0301-9322(93)90072-3.

Bragg, S. L., 1960. Effect of compressibility on the discharge coefficient of orifices and convergent nozzles. *J. Mech. Eng. Sci.* 2 (1), 35–44. doi:10.1243/JMES_JOUR_1960_002_007_02.

Brown, S., Martynov, S., Mahgerefteh, H., 2015. Simulation of two-phase flow through ducts with discontinuous cross-section. *Comput. Fluids* 120, 46–56. doi:10.1016/j.compfluid.2015.07.018.

Brown, S., Martynov, S., Mahgerefteh, H., Proust, C., 2013. A homogeneous relaxation flow model for the full bore rupture of dense phase CO_2 pipelines. *Int. J. Greenh. Gas Con.* 17, 349–356. doi:10.1016/j.ijggc.2013.05.020.

Chapman, C. J., 2000. *High Speed Flow*. Cambridge University Press, Cambridge, UK. ISBN 0-521-66647-3.

De Lorenzo, M., Lafon, P., Seynhaeve, J.-M., Bartosiewicz, Y., 2017. Benchmark of delayed equilibrium model (DEM) and classic two-phase critical flow models against experimental data. *Int. J. Multiphase Flow* 92, 112–130. doi:10.1016/j.ijmultiphaseflow.2017.03.004.

Debenedetti, P. G., 1997. *Metastable Liquids: Concepts and Principles*. Princeton University Press. ISBN 9780691213941. doi:10.1515/9780691213941.

Downar-Zapolski, P., Bilicki, Z., Bolle, L., Franco, J., 1996. The non-equilibrium relaxation model for one-dimensional flashing liquid flow. *Int. J. Multiphase Flow* 22 (3), 473–483. doi:10.1016/0301-9322(95)00078-X.

ECCSEL, 2021. Depressurization facility. https://www.eccsel.org/catalogue/113. Accessed 2021-12-07.

Edenhofer, O., Pichs-Madruga, R., Sokona, Y., Farahani, E., Kadner, S., Seyboth, K., Adler, A., Baum, I., Brunner, S., Eickemeier, P., Kriemann, B., Savolainen, J., Schlømer, S., von Stechow, C., Zwickel, T., (eds.), J. M., 2014. *Climate Change 2014: Mitigation of Climate Change*. Tech. rep., Working Group III Contribution to the Fifth Assessment Report of the Intergovernmental Panel on Climate Change, Summary for Policymakers, IPCC. URL http://mitigation2014.org/.

Edlebeck, J., Nellis, G. F., Klein, S. A., Anderson, M. H., Wolf, M., 2014. Measurements of the flow of supercritical carbon dioxide through short orifices. *J. Supercrit. Fluid.* 88, 17–25. doi:10.1016/j.supflu.2014.01.008.

Elias, E., Lellouche, G. S., Aug. 1994. Two-phase critical flow. *Int. J. Multiphase Flow* 20 (suppl.), 91–168. doi:10.1016/0301-9322(94)90071-X.

Fan, X., Wang, Y., Zhou, Y., Chen, J., Huang, Y., Wang, J., 2018. Experimental study of supercritical CO_2 leakage behavior from pressurized vessels. *Energy* 150, 342–350. doi:10.1016/j.energy.2018.02.147.

Fenghour, A., Wakeman, W. A., Vesovic., V., 1998. The viscosity of carbon dioxide. *J. Phys. Chem. Ref. Data* 27(1), 31–44. doi:10.1063/1.556013.

Flåtten, T., Lund, H., Dec. 2011. Relaxation two-phase flow models and the subcharacteristic condition. *Math. Mod. Meth. Appl. S.* 21 (12), 2379–2407. doi:10.1142/S0218202511005775.

Friedel, L., Jun. 1979. Improved friction pressure drop correlations for horizontal and vertical two phase pipe flow. In: *Proceedings, European Two Phase Flow Group Meeting*. Ispra, Italy. Paper E2.

Guo, X., Yan, X., Yu, J., Yang, Y., Zhang, Y., Chen, S., Mahgerefteh, H., Martynov, S., Collard, A., Jan. 2017. Pressure responses and phase transitions during the release of high pressure CO_2 from a large-scale pipeline. *Energy* 118, 1066–1078. doi:10.1016/j.energy.2016.10.133.

Guo, X., Yan, X., Yu, J., Zhang, Y., Chen, S., Mahgerefteh, H., Martynov, S., Collard, A., Proust, C., Sep. 2016. Pressure response and phase transition in supercritical CO_2 releases from a large-scale pipeline. *Appl. Energ.* 178, 189–197. doi:10.1016/j.apenergy.2016.06.026.

Hammer, M., Aasen, A., Wilhelmsen, Ø., 2020. Thermopack. https://github.com/SINTEF/thermopack/. Accessed 2020-12-15.

Hammer, M., Ervik, Å., Munkejord, S. T., 2013. Method using a density-energy state function with a reference equation of state for fluid-dynamics simulation of vapor-liquid-solid carbon dioxide. *Ind. Eng. Chem. Res.* 52 (29), 9965–9978. doi:10.1021/ie303516m.

Hendricks, R. C., Simoneau, R. J., Ehlers, R. C., Aug. 1972. *Choked flow of fluid nitrogen with emphasis on the thermodynamic critical region*. Technical Memorandum TM X-68107, National Aeronautics and Space Administration (NASA), Cleveland, Ohio, USA. URL https://ntrs.nasa.gov/citations/19720020638.

Henry, R. E., Fauske, H. K., 1971. The two-phase critical flow of one-component mixtures in nozzles, orifices, and short tubes. *J. Heat Transfer* 93, 179.

Hesson, J. C., Peck, R. E., 1958. Flow of two-phase carbon dioxide through orifices. *AIChE Journal* 4 (2), 207–210. doi:10.1002/aic.690040216.

IEA, 2021. *Net Zero by 2050 – A Roadmap for the Global Energy Sector*. IEA, Paris. URL https://www.iea.org/reports/net-zero-by-2050.

Kunz, O., Wagner, W., October 2012. The GERG-2008 wide-range equation of state for natural gases and other mixtures: An expansion of GERG-2004. *J. Chem. Eng. Data* 57 (11), 3032–3091. doi:10.1021/je300655b.

Lackme, C., 1979. Incompleteness of the flashing of a supersaturated liquid and sonic ejection of the produced phases. *Int. J. Multiphase Flow* 5 (2), 131–141. doi:10.1016/0301-9322(79)90041-7.

Li, K., Zhou, X., Tu, R., Xie, Q., Yi, J., Jiang, X., Jan. 2016. An experimental investigation of supercritical CO_2 accidental release from a pressurized pipeline. *J. Supercrit. Fluid.* 107, 298–306. doi:10.1016/j.supflu.2015.09.024.

Liao, Y., Lucas, D., Aug. 2017. Computational modelling of flash boiling flows: A literature survey. *Int. J. Heat Mass Tran.* 111, 246–265. doi:10.1016/j.ijheatmasstransfer.2017.03.121.

Lienhard, J. H., V, Lienhard, J. H., (IV), Mar. 1984. Velocity coefficients for free jets from sharp-edged orifices. *J. Fluids Eng.* 106 (1), 13–17. doi:10.1115/1.3242391.

Log, A. M., Munkejord, S. T., Hammer, M., 2021. HLLC-type methods for compressible two-phase flow in ducts with discontinuous area changes. *Comput. Fluids* 227. doi:10.1016/j.compfluid.2021.105023.

Martin, K., Rieberer, R., Hager, J., Jul. 2006. Modeling of short tube orifices for CO_2. In: *International Refrigeration and Air Conditioning Conference*. Purdue University. Paper 781.

Martynov, S., Zheng, W., Mahgerefteh, H., Brown, S., Hebrard, J., Jamois, D., Proust, C., 2018. Computational and experimental study of solid-phase formation during the decompression of high-pressure

CO_2 pipelines. *Ind. Eng. Chem. Res.* 57 (20), 7054–7063. doi:10.1021/acs.iecr.8b00181.
Moody, F. J., Feb. 1965. Maximum flow rate of a single component, two-phase mixture. *J. Heat Transfer* 87 (1), 134–141. doi:10.1115/1.3689029.
Munkejord, S. T., Austegard, A., Deng, H., Hammer, M., Stang, H. G. J., Løvseth, S. W., Nov. 2020. Depressurization of CO_2 in a pipe: High-resolution pressure and temperature data and comparison with model predictions. *Energy* 211, 118560. doi:10.1016/j.energy.2020.118560.
Munkejord, S. T., Deng, H., Austegard, A., Hammer, M., Skarsvåg, H. L., Aasen, A., Jul. 2021. Depressurization of CO_2-N_2 and CO_2-He in a pipe: Experiments and modelling of pressure and temperature dynamics. *Int. J. Greenh. Gas Con.* 109, 103361. doi:10.1016/j.ijggc.2021.103361.
Munkejord, S. T., Hammer, M., Jun. 2015. Depressurization of CO_2-rich mixtures in pipes: Two-phase flow modelling and comparison with experiments. *Int. J. Greenh. Gas Con.* 37, 398–411. doi:10.1016/j.ijggc.2015.03.029.
Munkejord, S. T., Hammer, M., Løvseth, S. W., May 2016. CO_2 transport: Data and models – A review. *Appl. Energ.* 169, 499–523. doi:10.1016/j.apenergy.2016.01.100.
Nakagawa, M., Berana, M. S., Kishine, A., 2009. Supersonic two-phase flow of CO_2 through converging-diverging nozzles for the ejector refrigeration cycle. *Int. J. Refrig.* 32 (6), 1195–1202. doi:10.1016/j.ijrefrig.2009.01.015.
Picard, D. J., Bishnoi, P. R., 1988. The importance of real-fluid behavior and nonisentropic effects in modeling decompression characteristics of pipeline fluids for application in ductile fracture propagation analysis. *Can. J. Chem. Eng.* 66 (1), 3–12. doi:10.1002/cjce.5450660101.
Pinhasi, G. A., Ullmann, A., Dayan, A., Aug. 2005. Modeling of flashing two-phase flow. *Reviews in Chemical Engineering* 21 (3-4), 133–264. doi:10.1515/REVCE.2005.21.3-4.133.
Rathjen, W., Straub, J., 1977. Temperature dependence of surface tension, coexisting curve, and vapor pressure of CO_2, $CClF_3$, $CBrF_3$, and SF_6. In: Hahne, E., Grigull, U. (Eds.), *Heat Transfer in Boiling*, Taylor & Francis Inc., chap. 18. ISBN 0-123-14450-7.
Ringstad, K. E., Allouche, Y., Gullo, P., Ervik, Å., Banasiak, K., Hafner, A., Dec. 2020. A detailed review on CO_2 two-phase ejector flow modeling. *Therm. Sci. Eng. Prog.* 20, 100647. doi:10.1016/j.tsep.2020.100647.
Roussanaly, S., Deng, H., Skaugen, G., Gundersen, T., 2021. At what pressure shall CO_2 be transported by ship? An in-depth cost comparison of 7 and 15 barg shipping. *Energies* 14 (18), 271–280. doi:10.3390/en14185635.
Shin, T. S., Jones, O. C., 1993. Nucleation and flashing in nozzles – 1. A distributed nucleation model. *Int. J. Multiphase Flow* 19 (6), 943–964. doi:10.1016/0301-9322(93)90071-2.
Span, R., Wagner, W., Nov.–Dec. 1996. A new equation of state for carbon dioxide covering the fluid region from the triple-point temperature to 1100 K at pressures up to 800 MPa. *J. Phys. Chem. Ref. Data* 25 (6), 1509–1596. doi:10.1063/1.555991.
Tesař, V., Nov. 2008. Characterisation of subsonic axisymmetric nozzles. *Chem. Eng. Res. Des.* 8 (11), 1253–1262. doi:10.1016/j.cherd.2008.04.012.
Toro, E. F., Billett, S. J., Nov. 2000. Centred TVD schemes for hyperbolic conservation laws. *IMA J. Numer. Anal.* 20 (1), 47–79. doi:10.1093/imanum/20.1.47.
Vree, B., Ahmad, M., Buit, L., Florisson, O., Oct. 2015. Rapid depressurization of a CO_2 pipeline – experimental study. *Int. J. Greenh. Gas Con.* 41, 41–49. doi:10.1016/j.ijggc.2015.06.011.
Wilhelmsen, Ø., Aasen, A., 2022. Choked liquid flow in nozzles: Crossover from heterogeneous to homogeneous cavitation and insensitivity to depressurization rate. *Chem. Eng. Sci.* 248, 117176. doi:10.1016/j.ces.2021.117176.
Wilhelmsen, Ø., Aasen, A., Skaugen, G., Aursand, P., Austegard, A., Aursand, E., Gjennestad, M. A., Lund, H., Linga, G., Hammer, M., 2017. Thermodynamic modeling with equations of state: Present challenges with established methods. *Ind. Eng. Chem. Res.* 56 (13), 3503–3515. doi:10.1021/acs.iecr.7b00317.
Yan, X., Guo, X., Yu, J., Chen, S., Zhang, Y., Mahgerefteh, H., Martynov, S., Brown, S., 2018. Flow characteristics and dispersion during the vertical anthropogenic venting of supercritical CO_2 from an industrial scale pipeline. In: Yan, J., Feitz, A., Li, X., Zhang, X. (Eds.), *Applied Energy Symposium and Forum, Carbon Capture, Utilization and Storage, CCUS 2018*. Energy Procedia, vol. 154, Perth, Australia, pp. 66–72. doi:10.1016/j.egypro.2018.11.012.